Human Molecular Genetics, 2018, Vol. 27, No.16 2893–2912

doi: 10.1093/hmg/ddy202
Advance Access Publication Date: 30 May 2018
Original Article

ORIGINAL ARTICLE

TSPO–PET imaging using [^{18}F]PBR06 is a potential translatable biomarker for treatment response in Huntington's disease: preclinical evidence with the p75^{NTR} ligand LM11A-31

Danielle A. Simmons[1,*,†], Michelle L. James[1,2,†], Nadia P. Belichenko[1], Sarah Semaan[1], Christina Condon[1], Jason Kuan[1], Adam J. Shuhendler[2], Zheng Miao[2], Frederick T. Chin[2] and Frank M. Longo[1]

[1]Department of Neurology and Neurological Sciences, Stanford University School of Medicine, Stanford, CA 94305, USA and [2]Department of Radiology, Molecular Imaging Program at Stanford, Stanford University, Stanford, CA 94305, USA

*To whom correspondence should be addressed. 1201 Welch Dr., MSLS P252, Stanford, CA 94305, USA. Tel: +1 6507360770; Fax: 650-498-4579; Email: simmons3@stanford.edu

Abstract

Huntington's disease (HD) is an inherited neurodegenerative disorder that has no cure. HD therapeutic development would benefit from a non-invasive translatable biomarker to track disease progression and treatment response. A potential biomarker is using positron emission tomography (PET) imaging with a translocator protein 18 kDa (TSPO) radiotracer to detect microglial activation, a key contributor to HD pathogenesis. The ability of TSPO–PET to identify microglial activation in HD mouse models, essential for a translatable biomarker, or therapeutic efficacy in HD patients or mice is unknown. Thus, this study assessed the feasibility of utilizing PET imaging with the TSPO tracer, [^{18}F]PBR06, to detect activated microglia in two HD mouse models and to monitor response to treatment with LM11A-31, a p75^{NTR} ligand known to reduce neuroinflammation in HD mice. [^{18}F]PBR06-PET detected microglial activation in striatum, cortex and hippocampus of vehicle-treated R6/2 mice at a late disease stage and, notably, also in early and mid-stage symptomatic BACHD mice. After oral administration of LM11A-31 to R6/2 and BACHD mice, [^{18}F]PBR06-PET discerned the reductive effects of LM11A-31 on neuroinflammation in both HD mouse models. [^{18}F]PBR06-PET signal had a spatial distribution similar to *ex vivo* brain autoradiography and correlated with microglial activation markers: increased IBA-1 and TSPO immunostaining/blotting and striatal levels of cytokines IL-6 and TNFα. These results suggest that [^{18}F]PBR06-PET is a useful surrogate marker of therapeutic efficacy in HD mice with high potential as a translatable biomarker for preclinical and clinical HD trials.

†The authors wish it to be known that, in their opinion, the first 2 authors should be regarded as joint First Authors.

Received: February 20, 2018. **Revised:** May 4, 2018. **Accepted:** May 21, 2018

Introduction

Huntington's disease (HD) is a fatal neurodegenerative disorder clinically characterized by progressive motor, psychiatric and cognitive deficits. The disease is caused by an expanded CAG repeat in the HTT gene encoding the huntingtin protein (1–4). The clinical manifestations are primarily attributed to preferential degeneration of the striatum as well as cortex and hippocampus. No therapy capable of delaying HD onset or slowing its progression exists. The pursuit of disease-modifying therapeutics would profit from the advent of mouse-to-human translatable biomarkers that enable treatment response to be measured.

Many of the identified mechanisms underlying HD neurodegeneration are associated with mutant huntingtin induced loss of neurotrophic support, primarily owing to disrupted brain-derived neurotrophic factor (BDNF) receptor signaling (5–10). Dysregulation of BDNF signaling via its tropomyosin receptor kinase B (TrkB) receptor has a well-characterized role in many aspects of HD pathogenesis (3,8) and more recent evidence suggests that degenerative patterns of $p75^{NTR}$ signaling are also fundamentally implicated (5–7,10–14). This dysfunctional $p75^{NTR}$ signaling has a causal link to HD-related structural (dendritic spine loss) and functional (long-term potentiation, cognition and motor ability) plasticity deficits in corticostriatum and hippocampus (5–7,12). Thus, $p75^{NTR}$ signaling has emerged as a target for HD therapeutics. Our laboratory developed a small molecule ligand, LM11A-31, that selectively binds $p75^{NTR}$ to activate trophic, while inhibiting degenerative, signaling (15,16). Preclinical testing in the R6/2 and BACHD mouse models of HD revealed that LM11A-31 normalized $p75^{NTR}$ receptor signaling, improved motor and cognitive performance, and reduced hallmark HD pathologies, including intranuclear huntingtin aggregates, dendritic spine loss and microglial activation. Moreover, LM11A-31 also increased the survival rate of R6/2 mice (7). These results establish small molecule $p75^{NTR}$ ligands as viable HD therapeutics and prime LM11A-31 for HD clinical testing since the compound is in Phase IIa clinical trials for mild to moderate Alzheimer's disease (ClinicalTrials.gov: NCT03069014).

Future plans for HD clinical testing of LM11A-31 and continued investigations toward developing other HD therapeutics would greatly benefit, at both preclinical and clinical stages, from non-invasive biomarkers related to known HD mechanisms that can track disease progression and therapeutic efficacy. Such markers are not necessarily expected to serve as diagnostic tools for HD since genetic testing along with clinical assessment can be used for a decisive diagnosis. Many effective clinical, cognitive, biochemical and neuro-/molecular imaging biomarkers of disease progression in HD patients have been identified (17–23). However, few, if any of these, have been validated for their usefulness in tracking therapeutic response in animal models and HD patients, a necessity for preclinical to clinical translation (19,20,24,25). Identifying such biomarkers is an urgent priority in HD translational research, particularly for therapies intended to delay or prevent symptom onset in premanifest HD gene carriers.

A molecular imaging biomarker that has been used successfully to indicate disease state in HD patients is positron emission tomography (PET) imaging using radiotracers targeting the translocator protein 18 kDa (TSPO). TSPO is mitochondrial membrane receptor located in cells throughout the body including the brain, in which it is present primarily in microglia (26–28). TSPO expression under normal physiologic conditions is low, however, it is up-regulated with injury and neuroinflammation (29), including in the striatum and cortex of HD patients (30), and has been used as a marker of microglial activation (31,32). Mutant huntingtin-induced microglial activation is progressive in the brains of HD patients and mouse models beginning in pre-symptomatic and/or early disease stages and has a key role in HD pathogenesis (33–40). TSPO is currently the best characterized molecular target for PET imaging of neuroinflammation, and, to date, five studies of HD patients have employed this technique using the most widely evaluated first generation TSPO radiotracer [^{11}C]PK11195 (41–45). [^{11}C]PK11195-PET imaging revealed elevated microglial activation in premanifest HD patients ~15 years before predicted symptom onset and the PET signal correlated with disease severity and cognitive dysfunction at manifest stages (42–46). These studies indicate that TSPO–PET imaging may be a valuable biomarker to monitor HD progression and therapeutic efficacy, however the latter indication and preclinical efficacy has yet to be examined. Furthermore, several second generation TSPO–PET radiotracers including [^{18}F]PBR06 (47–50), have been developed with superior sensitivity compared with [^{11}C]PK11195 (51–64), but these radiotracers have not yet been explored in HD.

Accordingly, the current study investigated whether the reductive effects of LM11A-31 on microglial activation in R6/2 and BACHD mouse models of HD could be detected with PET imaging using a second generation TSPO ligand, [^{18}F]PBR06. [^{18}F]PBR06 has been used in human studies and has a longer half-life, higher affinity and better signal-to-noise ratio than [^{11}C]PK11195 (48,50). Here, we show that [^{18}F]PBR06-PET signal was elevated in HD-affected brain areas of R6/2 mice at a late disease stage, and, notably, also in early and mid-symptomatic BACHD mice, compared with their respective age-matched wild-types (WTs). LM11A-31 treatment significantly reduced [^{18}F]PBR06 accumulation in each mouse model examined. The proof-of-concept data in this report are the first to demonstrate that TSPO–PET imaging can be used to detect increased microglial activation in HD mouse models and to evaluate efficacy of a putative HD therapeutic in either a preclinical or clinical context.

Results

[^{18}F]PBR06 PET imaging detects elevated microglial activation in R6/2 mice

Before investigating whether PET imaging with [^{18}F]PBR06 can be used to monitor LM11A-31 treatment response, initial studies were performed to determine whether this non-invasive imaging technique can enable specific and sensitive detection of TSPO changes in brains of living R6/2 mice. R6/2 mice are transgenic for the 5′ end of the human HD gene carrying 100–150 glutamine (CAG) repeats, develop progressive HD symptoms rapidly starting at ~5 weeks of age, show signs of striatal microglial activation at 5–7 weeks old, and striatal atrophy at 11–12 weeks old (33,65). Dynamic PET imaging was performed to study the uptake and kinetics of [^{18}F]PBR06 in male R6/2 mice at an advanced disease stage (11–12 weeks old). Time–radioactivity curves generated from these PET scans showed that, relative to age- and gender-matched WT littermates, R6/2 mice had greater initial uptake of [^{18}F]PBR06 in the forebrain (Fig. 1A) and predefined regions of interest: striatum, cortex and hippocampus (Fig. 1B–D), that are known to have increased reactive microglia in HD mouse models, including R6/2 mice (7,66,67). The

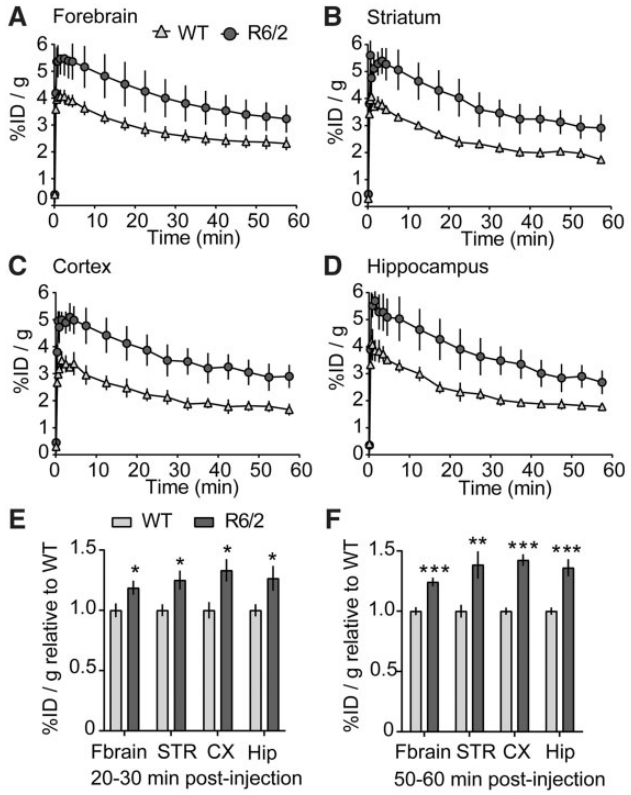

Figure 1. [^{18}F]PBR06-PET imaging detects elevated TSPO in brains of 11- to 12-week-old R6/2 mice. Time–radioactivity curves depicting [^{18}F]PBR06 uptake [% injected dose/gram (%ID/g)] in the forebrain (Fbrain; **A**), striatum (STR; **B**), cortex (CX; **C**), and hippocampus (Hip; **D**) of 11- to 12-week-old R6/2 mice ($n = 4$) and their WT littermates ($n = 3$). (**E**) Quantification of [^{18}F]PBR06 accumulation showed that uptake was significantly higher in R6/2 mice versus WTs ($n = 3$ and 4 mice, respectively) at 20–30 min post-injection of radiotracer in the forebrain and each predefined region of interest. (**F**) [^{18}F]PBR06 uptake remained significantly higher in R6/2 mice at 50–60 min when combined with 10 min static scans acquired at ∼50 min post-tracer injection ($n = 5$ WT mice; $n = 7$ R6/2 mice). Results are expressed as %ID/g mean ± s.e.m. Data were normalized to WT mice within each PET scan in (E) and (F) to minimize variability between imaging sessions. Statistical significance was determined with a two-tailed Mann–Whitney *U* test in (E) and a two-tailed Student's *t*-test in (F). $^{*}P \leq 0.05$, $^{**}P \leq 0.01$, $^{***}P \leq 0.001$ versus WT.

increased uptake was maintained in the R6/2 brain throughout the scan. Quantification of PET images revealed that [^{18}F]PBR06 accumulation in each brain area examined was significantly higher in R6/2 mice by ∼25–30% compared with WTs at 20–30 min post-injection of radiotracer (Fig. 1E) and remained higher at 50–60 min (Fig. 1F). These results indicate that [^{18}F]PBR06-PET is sufficiently sensitive to detect elevated TSPO, indicative of microglial activation, in 11- to 12-week old R6/2 mice.

[^{18}F]PBR06 specificity, *in vivo* biodistribution, and image quantification considerations

The *in vivo* specificity of the elevated PET signal in R6/2 mouse brain was investigated by assessing the extent that unlabeled PK11195 (1 mg/kg), which binds to the target of interest but is structurally different from [^{18}F]PBR06, inhibits [^{18}F]PBR06 binding to TSPO. Pre-blocking with PK11195 10 min before radiotracer injection greatly attenuated [^{18}F]PBR06 accumulation in mice of both genotypes and eliminated the significant increase seen in R6/2 mice (Supplementary Material, Fig. S1A–C). Reductions of ∼39–45% were seen in both WT and R6/2 mice in each brain region examined at 20–30 min post-tracer injection (for forebrain, $P = 0.006$, $n = 5$ WT and R6/2 mice combined, two-tailed Student's *t*-test) indicating appropriate specificity of [^{18}F]PBR06 in these mice.

Since TSPO is expressed in healthy as well as injured peripheral organs and tissues in both rodents and humans (31,32), the *in vivo* biodistribution of [^{18}F]PBR06 was assessed in the heart, kidneys, and interscapular brown adipose tissue of WT and R6/2 mice. High [^{18}F]PBR06 concentrations were observed in heart and kidneys (Supplementary Material, Fig. S1D and E), as expected of organs rich in TSPO, and lower in adipose tissue in mice of both genotypes. This peripheral biodistribution pattern is consistent with previous *ex vivo* studies of TSPO localization and *in vivo* accumulation of [^{18}F]PBR06 and other TSPO radiotracers in mice (47,68–70), which again attests to tracer specificity. While WT and R6/2 mice had similar [^{18}F]PBR06 uptake in heart and kidneys, R6/2 mice had significantly higher tracer accumulation in adipose tissue (Supplementary Material, Fig. S1G). The increased tracer seen in adipose tissue could be owing to inflammation associated with mutant huntingtin injured adipocytes present in R6/2 mice which contribute to disrupted body weight regulation and wasting (71,72).

Discerning subtle and variable changes in brain TSPO–PET signal, as could potentially occur with compound treatment, usually necessitates the use of a reference tissue model, standardized uptake values (SUVs), or an arterial input function to reduce variability, improve signal-to-background ratios and provide more precise quantification. Assessing input function for quantitative PET analysis is very difficult to execute in small rodents as it involves arterial blood sampling or obtaining an image-derived input function using the left ventricle, which is confounded by the high TSPO binding of the myocardium (73–76). An appealing alternative to this method is to identify a reference region, within the brain or periphery, in which TSPO expression is low and does not vary between comparison groups. Whole brain, muscle, and thalamus have been used previously as reference regions in small animal TSPO–PET studies (47,69,75,77), thus [^{18}F]PBR06 uptake was assessed in these areas in WT and R6/2 mice. TSPO expression was low in forelimb muscle of both genotypes but was significantly higher in R6/2 mice [muscle %ID/g (mean ±S.E.M.): 1.1 ± 0.14 WT-vehicle ($n = 9$ mice) versus 1.7 ± 0.12 R6/2-vehicle ($n = 6$ mice) at 20–30 min post-tracer injection, $P = 0.03$, two-tailed Student's *t*-test]. Genotype differences in [^{18}F]PBR06 accumulation were also seen in forebrain (Fig. 1A, E and F) and thalamus {%ID/g [mean ± standard error of the mean (S.E.M.)]: 2.5 ± 0.24 WT-vehicle versus 4.1 ± 0.61 R6/2-vehicle at 20–30 min post-tracer injection, $n = 5$ mice/group, $P = 0.04$ two-tailed Student's *t*-test}, which precludes the use of these areas as reference regions. SUVs are commonly used as relative measures of PET tracer uptake and are useful for compensating for variable body weights, as the weights are used as a substitute for a distribution volume of tracer (77,78). They have been utilized in previous PET imaging studies in R6/2 mice (76,79) and may normalize the variable adipose tissue uptake of the radiotracer (78), as seen in this study (Supplementary Material, Fig. S1F). Thus, SUV measures were used to compare [^{18}F]PBR06 accumulation in WT and R6/2 mice and conferred less variability and increased the statistical significance of the genotype difference compared with the %ID/g values [for R6/2 forebrain (%WT, $n = 4$ mice), %ID/g: 118 ± 5.92

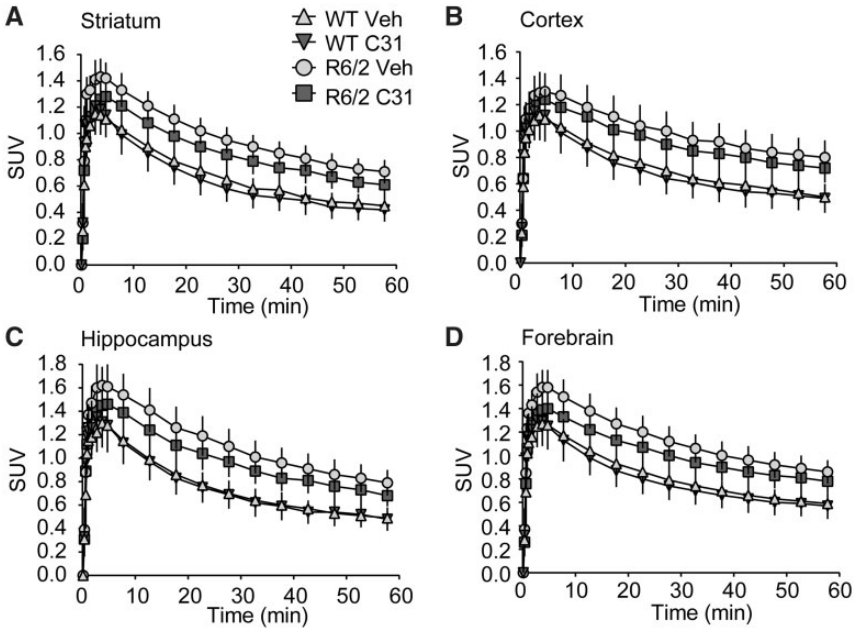

Figure 2. Kinetics of [^{18}F]PBR06 uptake in brains of WT and R6/2 mice with and without LM11A-31 treatment. Time–radioactivity curves from 60 min dynamic scans showing [^{18}F]PBR06 accumulation in the striatum (**A**), cortex (**B**), hippocampus (**C**) and forebrain (**D**) of 11- to 12-week-old WT and R6/2 mice treated with vehicle (Veh) or LM11A-31 (C31; $n = 4$–5 mice/group). Results are expressed as standardized uptake value (SUV) mean ± s.e.m.

(mean ± S.E.M.), $P = 0.04$; SUV: 116 ± 2.23, $P = 0.008$, both Student's *t*-test]. SUVs were therefore used as the measure to assess the therapeutic efficacy of LM11A-31 in subsequent experiments.

LM11A-31-associated reduction in activated microglia is detected with [^{18}F]PBR06-PET in R6/2 mice

Previous work from our laboratory showed that R6/2 mice treated with LM11A-31 (50 mg/kg once daily 5 days/week by oral gavage) for 7 weeks starting at 4 weeks of age reduced striatal and hippocampal microglial activation compared with those treated with vehicle (7). Here, we used the same compound administration paradigm to examine whether LM11A-31-associated reductions in activated microglia could be detected using [^{18}F]PBR06-PET imaging. Given that R6/2 mice show significant striatal and whole brain volume reductions at 11–12 weeks of age (65,80), MRIs were performed for each mouse and co-registered with PET/computed tomography (CT) images to ensure accurate delineation of volumes of interest (VOIs) in predefined brain regions.

Time–radioactivity curves from 60 min dynamic scans showed differential [^{18}F]PBR06 uptake between the genotypes (vehicle-treated WT and R6/2 mice) and vehicle and LM11A-31-treated R6/2 mice in striatum, cortex, hippocampus as well as forebrain (Fig. 2). Additional static scans (10 min duration starting ∼20 min post-tracer injection) were performed and data from these scans were combined with the appropriate timeframe from the dynamic scans for quantification. [^{18}F]PBR06-PET signal was increased in vehicle-treated R6/2 mice compared with WTs in each brain area examined (Fig. 3). LM11A-31 treatment significantly reduced [^{18}F]PBR06 uptake in R6/2 mice by ∼20% compared with vehicle administration (Fig. 3). These results indicate that, in 11- to 12-week old R6/2 mice, [^{18}F]PBR06-PET can discern the reductive effects of LM11A-31 on microglial activation in HD-affected brain areas.

[^{18}F]PBR06-PET detects ameliorative effects of LM11A-31 on microglial activation in BACHD mice

After obtaining the above positive results in late symptomatic R6/2 mice, it was of interest to determine whether TSPO–PET could also detect LM11A-31 effects at early and mid-symptomatic stages in the BACHD mouse model of HD using a cross-sectional study design. BACHD mice express full-length human mutant huntingtin and better represent the genetic component of HD (81). These mice have a slower disease progression than R6/2 mice with mild motor symptoms at 3 months of age that become more robust at 6–9 months (81–85). These symptoms occur before brain atrophy as BACHD mice fail to show striatal and cortical volume changes at 12- to 15-months old, as assessed with MRI (82). Previous reports from our laboratory showed that reactive microglia are present in BACHD mice in the striatum and hippocampus at 9 months of age (7,66). LM11A-31 (50 mg/kg once daily 5 days/week), administered orally for 7 months starting at 2 months of age, decreased microglial activation in BACHD mice compared with age-matched WTs (7). LM11A-31-treated BACHD mice showed reductions in other key HD neuropathologies in striatum and/or hippocampus (e.g. neurite degeneration and dendritic spine loss) and improved motor and cognitive function. Thus, we initially examined [^{18}F]PBR06 uptake in the 9-month-old BACHD mice described in the previous report (7).

Time–radioactivity curves showed elevated [^{18}F]PBR06 uptake in vehicle-treated BACHD mice at 9 months of age compared with WTs in each brain area examined and was reduced by LM11A-31 treatment (Supplementary Material, Fig. S2). Quantification of 10-min static scans started at ∼20 min after tracer injection combined with the comparable timeframe of the dynamic scans showed significantly increased [^{18}F]PBR06-PET signal in each VOI in BACHD-vehicle mice versus WTs (Fig. 4). LM11A-31 significantly attenuated this increase in the forebrain, striatum, cortex and hippocampus and showed a tendency to do so in the thalamus and hypothalamus of mid-symptomatic BACHD mice.

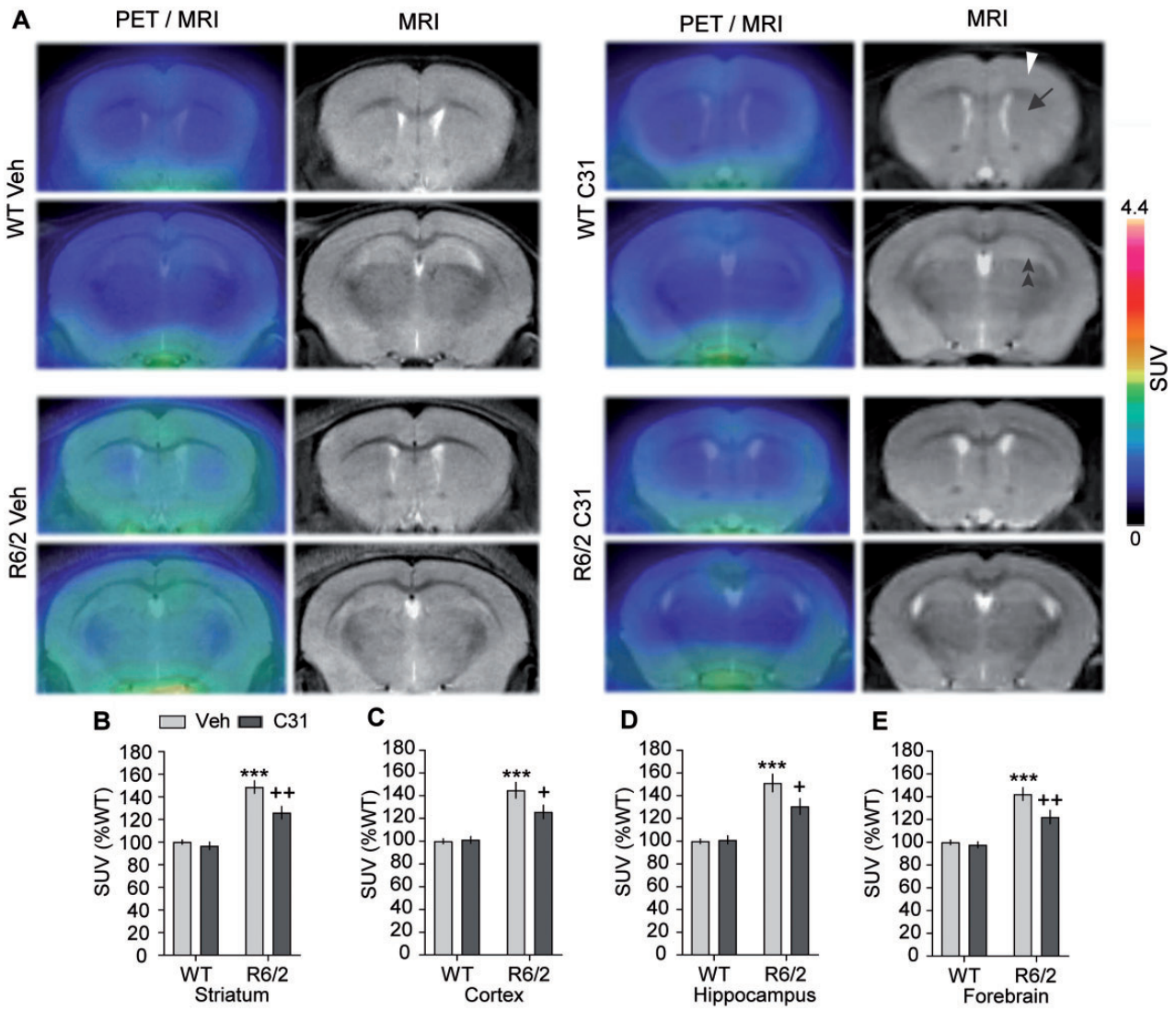

Figure 3. [^{18}F]PBR06-PET detects reduced TSPO levels in R6/2 mice treated with LM11A-31. (**A**) Representative PET and MR images of coronal sections of the striatum (black arrow), cortex (white arrowhead) and hippocampus (two black arrowheads) of WT and R6/2 mice with and without LM11A-31 (C31) treatment. PET/MRI overlay is in the left columns and MRI alone is in the right columns. (**B–E**) Quantification of [^{18}F]PBR06 uptake in striatum (**B**), cortex (**C**), hippocampus (**D**), and forebrain (**E**) of WT-Veh ($n = 14$), WT-C31 ($n = 8$), R6/2-Veh ($n = 10$) and R6/2-C31 ($n = 11$) groups. Results are expressed as standardized uptake value (SUV) mean ± s.e.m. and normalized to the PET signal of the WT-Veh within each group of four mice imaged at the same time to minimize variability between imaging sessions. Statistical significance was determined with an ANOVA and Fisher's LSD. $^{***}P < 0.0001$ versus WT-Veh; $^{+}P < 0.01$ and $^{++}P < 0.01$ versus R6/2-Veh.

Given the favorable results obtained in mid-symptomatic BACHD mice, we examined whether [^{18}F]PBR06-PET could distinguish earlier and more subtle changes in microglial activation in BACHD mice at 5 months of age when motor symptoms are mild and variable. Detection at early symptomatic stages is critical as therapeutics would be more effective in disease prevention if administered at pre- or early symptomatic stages. Importantly, [^{18}F]PBR06 accumulation was elevated in 5-month-old BACHD mice versus WTs in the forebrain as well as striatum, cortex, hippocampus and hypothalamus (Fig. 5; see Supplementary Material, Fig. S3 for time–radioactivity curves). LM11A-31 prevented the increase in tracer uptake in each of these brain regions. Thus, [^{18}F]PBR06-PET can detect increased TSPO levels at two disease stages in BACHD mice, including an early symptomatic stage, as well as LM11A-31 ameliorative effects on microglial activation at both stages of disease progression.

The *in vivo* biodistribution of [^{18}F]PBR06 in the heart, kidneys and adipose tissue of WT and BACHD mice at both 5 and 9 months of age is similar to known patterns of TSPO localization (47,68,69). [^{18}F]PBR06 uptake in BACHD mice was similar to WTs in heart and kidneys at both ages examined and 21 ± 7% greater in adipose tissue at 9 but not 5 months of age (Supplementary Material, Fig. S4). LM11A-31 treatment did not affect tracer uptake in the peripheral organs/tissue examined. As seen with the R6/2 mice, pre-blocking with unlabeled PK11195 greatly reduced [^{18}F]PBR06 accumulation in 9-month-old BACHD mice by 28–58% and eliminated the genotype difference in each brain area assessed (Supplementary Material, Fig. S5). To determine if the percentage of [^{18}F]PBR06 available for binding varied between the treatment groups, the plasma free fraction (f_P) of the tracer was measured in 9-month-old WT and BACHD mice with and without LM11A-31 treatment. Plasma protein binding was not affected by genotype or LM11A-31 as groups did not

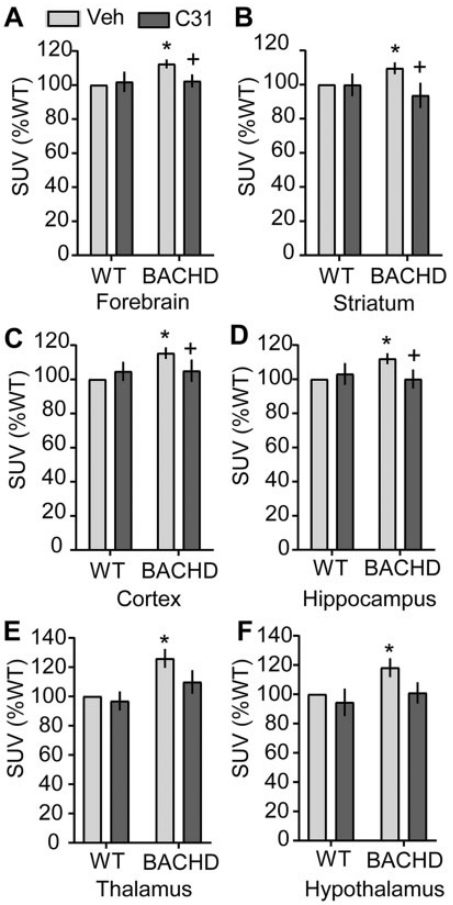

Figure 4. Microglial activation and LM11A-31's reductive effects are detected by [^{18}F]PBR06-PET in 9-month-old BACHD mice. Quantification of [^{18}F]PBR06 accumulation in predefined brain areas (**A–F**) of WT-Veh ($n = 11$), WT-C31 ($n = 12$), BACHD-Veh ($n = 13$) and BACHD-C31 ($n = 14$) mice (combined data from 10 min static scans acquired at ~20 min after tracer injection and appropriate timeframe of dynamic scans). Results are expressed as standardized uptake value (SUV) mean ± s.e.m. and were normalized to the WT-Veh group of the yoked PET scan. Statistical significance was determined with an ANOVA and Fisher's LSD. $^{*}P < 0.05$ versus WT-Veh; $^{+}P \leq 0.05$ versus BACHD-Veh.

significantly differ in f_P values (WT-vehicle: 69 ± 4; WT-LM11A-31: 71 ± 1; BACHD-vehicle: 70 ± 2; BACHD-LM11A-31: 66 ± 6; $n = 3$–5 mice/group).

Ex vivo autoradiography shows patterns of [^{18}F]PBR06 accumulation similar to those detected with *in vivo* microPET in R6/2 mice

Ex vivo autoradiography has much higher spatial resolution than microPET and was therefore used to further assess and corroborate the increased TSPO expression observed in specific brain regions after [^{18}F]PBR06-PET imaging. Autoradiography was performed on a subset of R6/2 mice (Fig. 6A) after 10-min static PET scans and compared with their respective age-matched WTs. Notable accumulation of radioactivity was seen in brain regions corresponding to those with increased [^{18}F]PBR06 uptake shown by PET imaging. Quantification of autoradiography images revealed significantly elevated [^{18}F]PBR06 in the striatum, cortex and hippocampus of vehicle-treated R6/2 mice compared with WTs that was reduced with LM11A-31 treatment (Fig. 6B–D). These *ex vivo* autoradiography results are consistent with the *in vivo* PET results in this study as well as post-mortem pathological studies of TSPO distribution and *in vivo* PET in HD patients (18,30). Moreover, the mean intensity of the autoradiography signal in the striatum, cortex and hippocampus significantly correlated with the [^{18}F]PBR06-PET signal in these brain regions (Fig. 6E–G).

LM11A-31-associated reductions in microglial activation correlate with decreases in [^{18}F]PBR06-PET signal

Microglial activation is a complex process involving changes in morphology, antigen/receptor expression, phagocytosis and cytokine release. As mentioned above, reactive microglia contain elevated TSPO levels and TSPO expression is up-regulated in striatum and cortex of HD patients (30) but has yet to be assessed in HD mouse models. Thus, postmortem assays of TSPO levels via Western immunoblotting were performed on striatal, cortical, and hippocampal lysates from the 11- to 12-week-old R6/2 mice and 9-month-old BACHD mice that were PET imaged. In R6/2 mice, TSPO levels in the striatum more than doubled compared with WTs and increased by 60–70% in the hippocampus and cortex (Fig. 7A–C). LM11A-31 significantly reduced TSPO levels in the striatum and cortex. TSPO levels were also significantly increased by 35% in the striatum and 22% in the hippocampus in 9-month-old BACHD mice versus age-matched WTs; the increase in the cortex did not reach statistical significance (Fig. 7D–F). BACHD mice treated with LM11A-31 had significantly lower TSPO levels in each brain area examined compared with those given vehicle.

IBA-1 is a protein expressed by activated or proliferating microglia that is up-regulated in HD patients and mouse models, including R6/2 and BACHD mice (33,67,86–88). Similar to our prior reports (7,66), increased striatal and hippocampal area occupied by IBA-1-stained microglia in vehicle-treated R6/2 mice that were PET imaged was decreased with LM11A-31 treatment; similar results were observed in the cortex (Fig. 7G–J). We previously published that elevated IBA-1 in the striatum and hippocampus was significantly decreased in the 9-month-old BACHD mice that were PET imaged in the current study (7). In the present study, a significant increase in IBA-1-immunostained area was also seen in the cortex of BACHD-vehicle mice compared with WT-vehicle mice that was ameliorated by LM11A-31 treatment [IBA-1-stained area (%WT): WT-vehicle, 100 ± 6.8; BACHD-vehicle, 113 ± 3.5; BACHD-LM11A-31, 102 ± 4; BACHD-vehicle versus WT-vehicle, $P = 0.05$; BACHD-vehicle versus BACHD-LM11A-31, $P = 0.04$; $n = 7$–10 mice/group].

Activated microglia release cytokines to mediate inflammatory responses and elevated cytokine levels are prevalent in the plasma and/or brains of HD patients and mouse models (39,89). Thus, the effects of LM11A-31 on cytokine levels was assessed in the striatum of R6/2 mice that underwent [^{18}F]PBR06-PET imaging. The relative concentrations of cytokines were measured using the antibody-based 38-plex Luminex array. Levels of 9 of the 38 cytokines measured were increased in the striatum of R6/2-vehicle mice compared with WTs (Fig. 8A–I): interleukin (IL)-6, tumor necrosis factor α (TNFα), IL-2, CXCL10, chemokine (C–C motif) ligand 5 (CCL5)/regulated on activation normal T cell expressed and secreted (RANTES), IL-1β, IL-22, transforming growth factor β (TGF- β) and interferon-γ (IFN-γ); and two were decreased (Fig. 8J and K): CCL11/eotaxin and vascular endothelial growth factor (VEGF). LM11A-31 prevented the increase in IL-6, TNFα, IL-2 and CXCL10 seen in the R6/2 striatum. While CCL2 was not significantly altered in R6/2-vehicle striatum

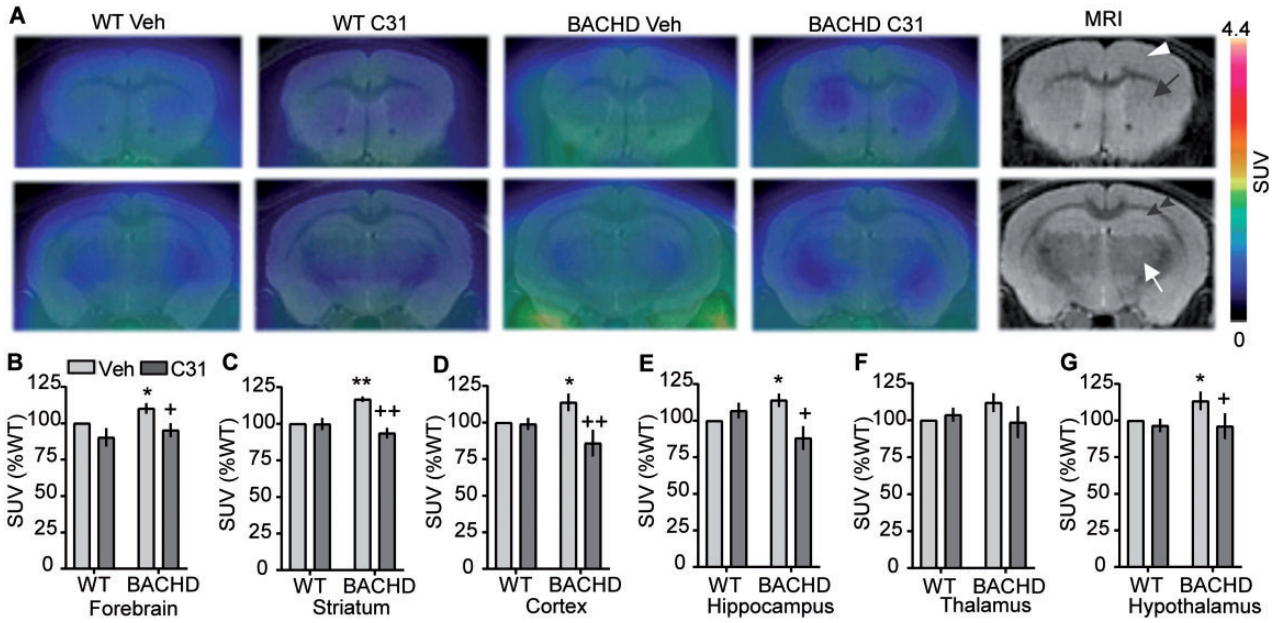

Figure 5. [18F]PBR06 accumulation is increased in 5-month-old BACHD mice and reduced with LM11A-31 treatment. (**A**) Representative PET and MR images of coronal sections of the striatum (black arrow), cortex (white arrowhead), hippocampus (two black arrowheads) and thalamus (white arrow) of WT and 5-month-old BACHD mice with and without LM11A-31 (C31) treatment. PET/MR image overlay is in the four left columns and MR image alone is in the right column. (**B–G**) Quantification of [^{18}F]PBR06 accumulation in predefined brain areas at ~20 min post-injection of radiotracer of 60 min dynamic scans ($n = 6$–8 mice/group). Results are expressed as standardized uptake value (SUV) mean ± s.e.m. and normalized to the WT-Veh mouse within each group of four mice imaged at the same time. Statistical significance was determined with an ANOVA and Fisher's LSD. $^{*}P \leq 0.05$ and $^{**}P \leq 0.01$ versus WT-Veh; $^{+}P \leq 0.05$ and $^{++}P \leq 0.01$ versus BACHD-Veh.

versus WTs, LM11A-31 decreased levels of CCL2 (Fig. 8L). The other cytokines did not significantly differ between the genotypes or with LM11A-31 treatment (Supplementary Material, Fig. S6). Overall, LM11A-31 decreased microglial activation, as evidenced by reductions in TSPO and IBA-1, and altered the functional phenotypes of microglia by reducing certain key pro-inflammatory cytokines and chemokines.

[^{18}F]PBR06-PET signal correlated strongly with TSPO levels in striatum, cortex and hippocampus ($r = 0.73$–0.76; Fig. 9A–C) and moderately with IBA-1 immunostaining ($r = 0.56$–0.69; Fig. 9D–F) of WT and R6/2 mice with and without LM11A-31 treatment ($n = 6$–10 mice/group). [^{18}F]PBR06-PET uptake also had a strong correlation with striatal levels of IL-6 ($r = 0.72$; Fig. 9G) and a less robust but significant association with TNFα ($r = 0.56$; Fig. 9H) but not with the other cytokines that had significant differences between genotypes and LM11A-31 treatment (IL-2: $r = 0.31$; CXCL10: $r = 0.33$, both $P = 0.12$).

TSPO is predominately located on activated microglia in the brain, however, depending on the type of neuronal injury, astrocytes also up-regulate the receptor (32,90,91). Since astrogliosis and astrocyte reactivity occur in brains of HD patients and mouse models at advanced disease stages (3,92), associations between levels of the astroglial marker, glial fibrillary acidic protein (GFAP) and [^{18}F]PBR06-PET signal were investigated in striatum of R6/2 mice. GFAP levels, as assessed with immunoblotting, did not significantly differ between the genotypes or with LM11A-31 treatment (data not shown) nor did they correlate with [^{18}F]PBR06 uptake (Fig. 9I). Previous reports showed a similar absence of astrogliosis in symptomatic R6/2 mice and lack of correlation between reactive astrocytes and TSPO–PET signal in human neurological diseases including Alzheimer's disease and amyotrophic lateral sclerosis (93,94). Since [^{18}F]PBR06 accumulation correlated with the microglial marker IBA-1 in this study as well as other markers of microglial activation in previous studies (26,75), the TSPO–PET signal most likely reflects activated microglia with a relatively minor contribution from astrocytes.

Discussion

The success rate of drug candidates in clinical trials for HD would be greatly augmented if trials were guided by translatable biomarkers that enable tracking of disease progression and treatment response. Said biomarkers with a strong link to known mechanisms of HD pathogenesis and detection sensitivity in early disease stages would be most effective, especially for evaluating therapies aiming to delay or prevent symptom onset in premanifest HD gene expansion carriers. In the current studies, we investigated whether TSPO–PET imaging could be a suitable translatable biomarker for detecting *in vivo* microglial activation, a key contributor to HD pathogenesis, in two HD mouse models at multiple disease stages, as it has been shown to do in HD patients (42,44–46). Furthermore, we assessed whether TSPO–PET using [^{18}F]PBR06-PET could be utilized to monitor response to treatment with LM11A-31, a small molecule p75^{NTR} ligand known to reduce HD-related neuroinflammation (7). The results of these experiments demonstrate that [^{18}F]PBR06-PET signal was elevated in the striatum, cortex and hippocampus of vehicle-treated R6/2 mice at a late disease stage compared with WTs and that LM11A-31 treatment significantly reduced [^{18}F]PBR06 binding. Notably, in cross-sectional studies, [^{18}F]PBR06-PET uptake was also significantly increased in early and mid-symptomatic BACHD mice in multiple HD-affected brain areas and ameliorative effects of LM11A-31 on neuroinflammation were also discerned. The [^{18}F]PBR06-PET signal correlated with other markers of microglial activation, including IBA-1 immunostaining, TSPO immunoblotting, and elevated striatal levels of cytokines IL-6 and TNFα. These results

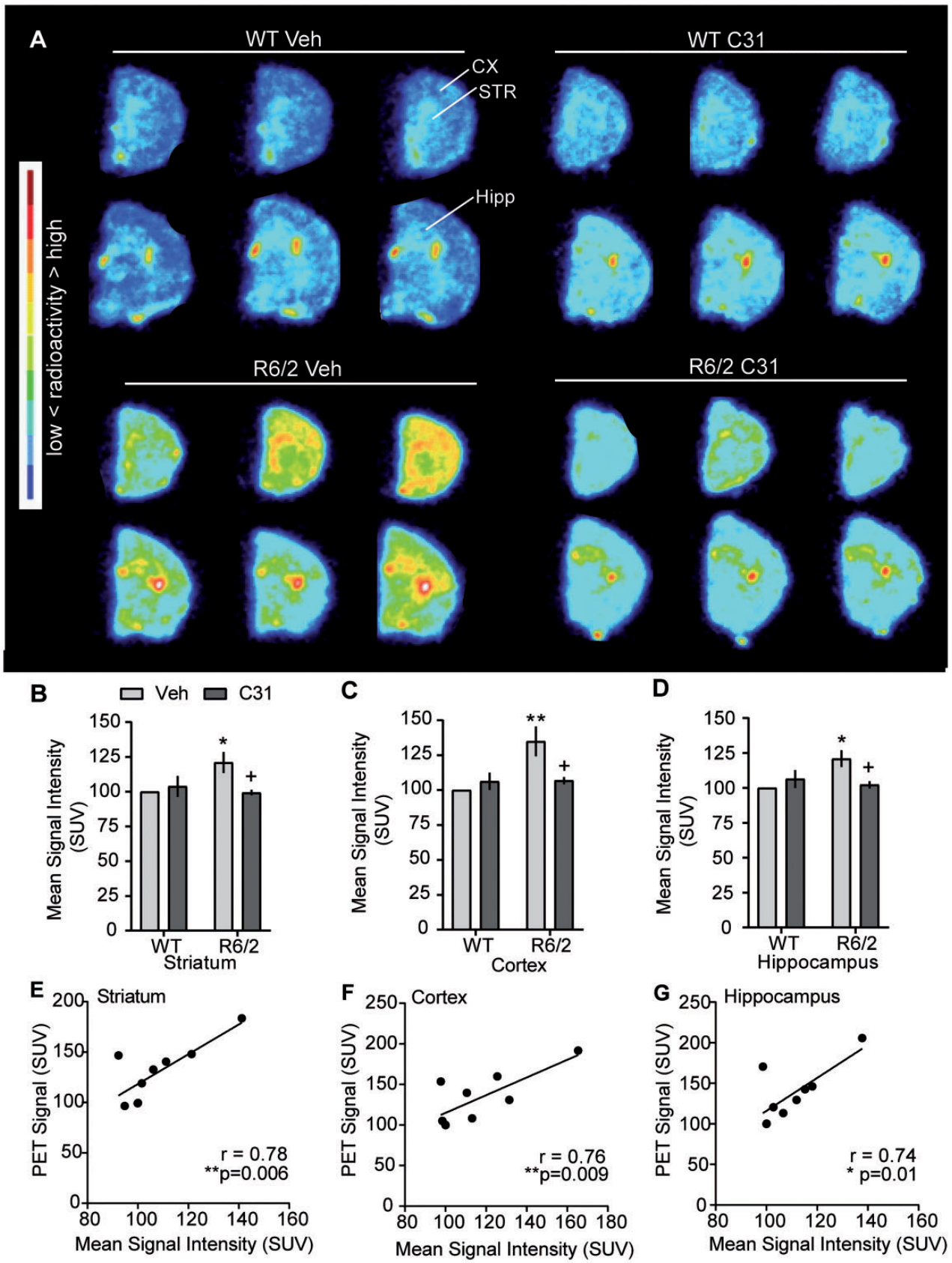

Figure 6. *Ex vivo* autoradiography showing regional [^{18}F]PBR06 uptake corresponding to *in vivo* PET results in R6/2 mice. (**A**) Representative autoradiography images demonstrating a regional pattern of [^{18}F]PBR06 uptake similar to that seen in PET images of WT and R6/2 mice treated with vehicle or LM11A-31. Sections from 4 mice (one from each treatment group in most instances) were arranged on each autoradiography film. Quantification of [^{18}F]PBR06 accumulation in striatum (STR; **B**), cortex

are the first to demonstrate that TSPO–PET imaging can be used to detect increased microglial activation in HD mouse models and to evaluate treatment response in HD preclinical or clinical testing. The proof-of-concept data obtained here provide a basis for future preclinical studies that will be critical in delineating the optimal TSPO–PET methods for detecting therapeutic efficacy of other putative HD treatments for ultimate translation to use in the clinic.

Previous human TSPO–PET studies using [^{11}C]PK11195 showed microglial activation in striatum, cortex, thalamus and hypothalamus (18,41–45), but not the hippocampus (44), in both premanifest and manifest HD gene expansion carriers. These results largely correspond with the regional patterns of increased [^{18}F]PBR06-PET signal seen in R6/2 and/or BACHD mice except that in the HD mouse models [^{18}F]PBR06 accumulation was also evident in the hippocampus. [^{18}F]PBR06 affords a higher signal-to-noise ratio than [^{11}C]PK11195 which could account for this difference. The spatial distribution of the *in vivo* PET signal in R6/2 and BACHD mice was in accord with that seen with *ex vivo* autoradiography and IBA-1 immunostaining. In studies of HD patients, the [^{11}C]PK11195-PET signal correlated with striatal dopamine receptor (D_2) loss and motor symptom severity in manifest stages (42), and with cognitive deficits in the associative striatum and an increased probability of symptom onset in premanifest stages (44,45). These results in HD patients, together with the findings of the current study, support the value of TSPO–PET imaging as an effective mouse-to-human translatable biomarker of disease progression and treatment response.

Importantly, [^{18}F]PBR06-PET enabled detection of microglial activation and reduced neuroinflammation following LM11A-31 treatment in HD-affected brain areas of BACHD mice at multiple disease stages, including early in disease progression at 5 months of age. At this age, BACHD mice show anxiety-like behavior as well as mild and variable motor deficits that emerge at 3 months of age and do not become pronounced until 6–9 months old (82–85). The known temporal sequence of neuropathological manifestations includes increased full-length huntingtin levels at 2 months old, decreased cortical and striatal BDNF levels decreases at 6–9 months of age, and dendritic spine loss at 9 months old (7,66,81,84). Until this study, the earliest age reported for reactive microglia in BACHD striatum was 9 months of age (7,66). These results contribute to a body of work showing that microglial activation is progressive in striatum and cortex of HD patients and mouse models beginning in presymptomatic and/or early stages indicating that inflammatory processes contribute to subclinical disease progression and are integral contributors to fundamental HD pathology (18,23,40,95). We previously showed that LM11A-31 reduced microglial activation, as assessed with IBA-1 immunostaining, in BACHD mice at 9 months of age (7) and here we show that, at this age and earlier at 5 months old, the reduction can also be distinguished with [^{18}F]PBR06-PET. Early detection of microglial activation and treatment effects by TSPO–PET imaging will be instrumental in evaluating the efficacy of neuroprotective strategies as therapeutics would be more effective in disease prevention or onset delay if applied at pre- or early-symptomatic stages.

Reactive microglia release neurotoxic pro-inflammatory cytokines that further activate microglia, creating a self-propagating cycle of inflammatory processes. Our results are the first to show that a distinct panel of cytokines/chemokines is altered in the R6/2 striatum. Striatal levels of IL-6, TNFα, IL-2, CXCL10, CCL5/RANTES, IL-1β, IL-22, TGF-β and IFN-γ were increased in R6/2 versus WT mice, while CCL11/eotaxin and VEGF were decreased. LM11A-31 prevented the increase in IL-6, TNFα, IL-2 and CXCL10 possibly via its inhibition of nuclear factor kappa B (NF-κB) signaling (7) and/or reduction of TSPO levels as seen in the present study. Signaling via the NF-κB pathway is increased in HD patients and mouse models and promotes cytokine expression (7,96–98) and TSPO has been functionally implicated in pro-inflammatory responses as it is located on classically activated M1 microglia and is involved in TNFα and nitric oxide (NO) production and up-regulation of IL-6 and inducible NO synthase expression (69,99–102). Pro-inflammatory cytokines are increased in HD brains including at premanifest stages and also show distinct patterns of elevation as opposed to general increases seen in other neurodegenerative diseases (103–105). Cytokine levels are also elevated in the CSF and plasma of HD patients and mouse models and increase significantly with disease progression, particularly IL-6 which was elevated in plasma ∼16 years before symptom onset in humans (103,106–110). Moreover, plasma levels of certain cytokines including TNFα and IL-6 correlated with [^{11}C]PK11195-PET signal in cortex of premanifest HD patients ∼10 years before predicted disease onset and has also been suggested as an HD biomarker (43). In our study, striatal IL-6 and TNFα levels correlated with the [^{18}F]PBR06-PET signal and future studies will examine whether plasma cytokine levels also do so.

Besides the current study, few other preclinical or clinical studies have assessed the usefulness of TSPO–PET in monitoring therapeutic efficacy despite its broad potential impact given the pervasiveness of neuroinflammation in neurodegenerative disorders and its established detection of glial activation in many of these conditions. These few studies showed that TSPO–PET detected microglial activation and treatment response in animal models of multiple sclerosis (111), spinal cord injury (112), Alzheimer's disease (75) and HD in this report, as well as in multiple sclerosis patients (113). The magnitude of the treatment response in these studies is similar to the 15–18% decrease in [^{18}F]PBR06 uptake seen with LM11A-31 treatment in this study. The scarcity of TSPO–PET studies monitoring treatment response could be owing to reported technical challenges encountered by small animal PET imaging and/or certain TSPO radioligands. One limitation in the preclinical milieu is the restricted spatial resolution of rodent PET scanners contributing to partial-volume effects when radiotracer uptake is quantified in small VOIs (114,115). However, anatomical confirmation of the PET signal using higher spatial resolution *in vivo* techniques (e.g. MRI) and *ex vivo* methods such as autoradiography utilized in this study, substantially aids quantification and interpretation of the results (75,115). Moreover, the use of ^{18}F-labeled radiotracers such as [^{18}F]PBR06 enables longer imaging sessions and higher resolution imaging compared with ^{11}C-labeled tracers owing to the longer half-life ($t_{1/2}$ = 110 versus 20 min) and low positron energy (0.63 MeV) of ^{18}F (51). The longer half-life of ^{18}F-labeled tracers also allows for study design flexibility, making large-scale rodent studies practical, and is advantageous for clinical translation as an on-site cyclotron is not required (116).

(CX; **C**), and hippocampus (Hipp; **D**). SUVs were computed using the mean signal intensity, decay corrected dose and body weight and normalized to the WT-Veh mouse on a given autoradiography film. *$P \leq 0.05$ and **$P \leq 0.01$ versus WT-Veh; $^{+}P \leq 0.05$ versus R6/2-Veh; $n = 4$–5 mice/group. Scatterplots with linear regression lines showing that the mean intensity of the autoradiography signal in STR (**E**), CX (**F**) and Hipp (**G**) significantly correlates with the [^{18}F]PBR06-PET signal in these brain regions ($n = 3$ mice/group, groups are combined for the analysis). Spearman rank-order correlation coefficients (r) and P values are shown.

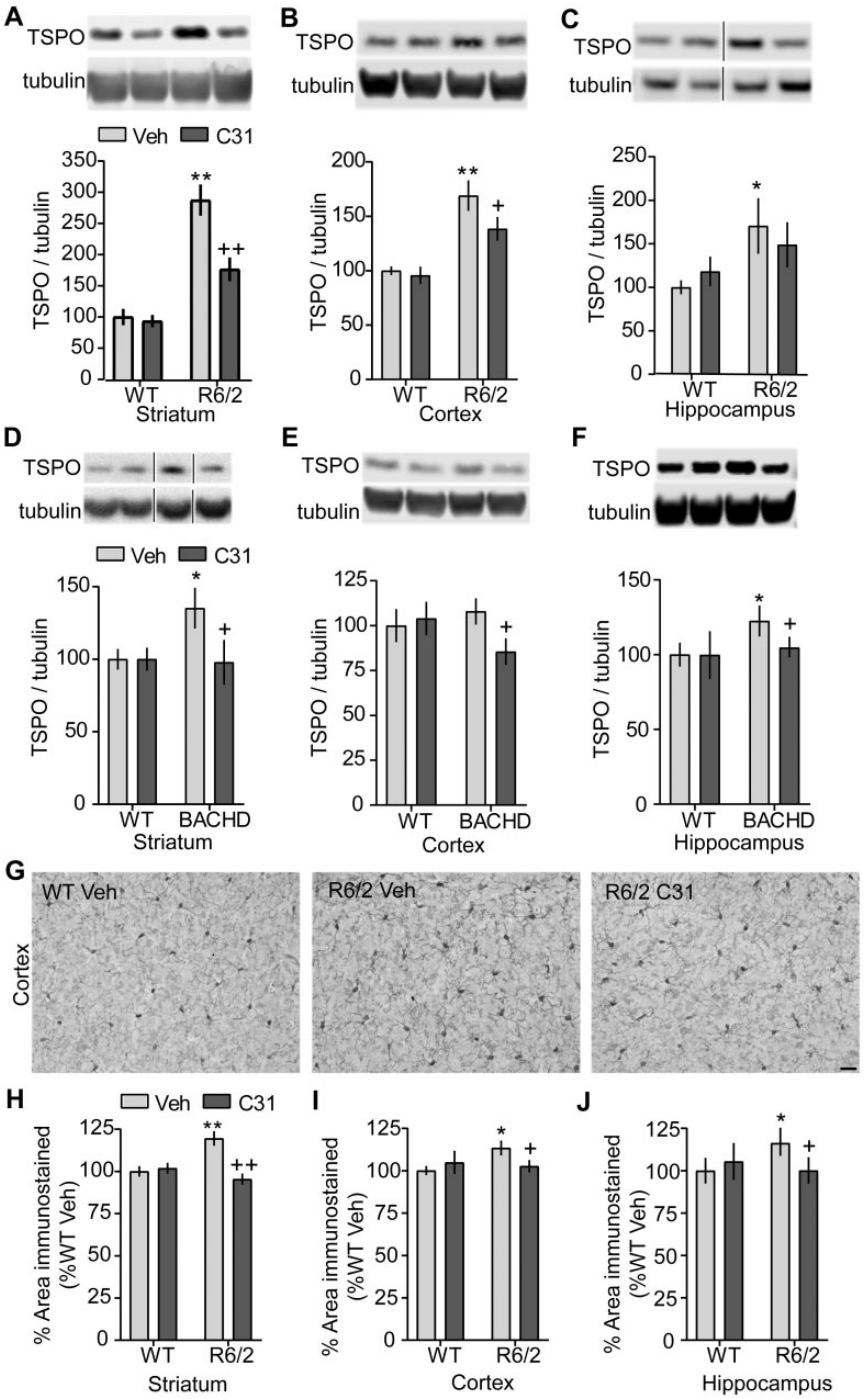

Figure 7. Microglial activation markers are reduced by LM11A-31 in brains of R6/2 and BACHD mice. (A–F) Representative western immunoblots for TSPO of striatal, cortical and hippocampal homogenates from vehicle (Veh)- or LM11A-31 (C31)-treated 11- to 12-week-old R6/2 mice (A–C), 9-month-old BACHD mice (D–F), and their respective age-matched WTs ($n = 9$–13 mice/group). Immunobands from one mouse per group and corresponding densitometric group analyses are shown. For all quantification, values were normalized to the WT-Veh group run on the same gel. For (A–F), $^{*}P \leq 0.05$ and $^{**}P \leq 0.0001$ versus WT-Veh; $^{+}P \leq 0.05$ and $^{++}P \leq 0.0001$ versus transgenic (R6/2 or BACHD)-Veh; ANOVA and Fisher's LSD. For comparison purposes, some non-adjacent lanes of the same gel were moved together and separated by thin black lines. (G) Representative photomicrographs of immunostaining for the microglial marker, IBA-1, in the cortex of a Veh-treated WT (left) and R6/2 mouse (middle), and a C31-treated R6/2 mouse (right; scale bar = 50 μm). Quantification of the area occupied by IBA-1-immunostained soma and processes in WT and R6/2 striatum (H), cortex (I) and hippocampus (J). All results are expressed as the mean ± s.e.m. Statistical significance was determined with an ANOVA and Fisher's LSD or Student's *t*-test. For (H–J), $^{*}P \leq 0.05$ and $^{**}P \leq 0.0001$ versus WT-Veh; $^{+}P \leq 0.05$ and $^{++}P \leq 0.0001$ versus R6/2-Veh; $n = 9$–15 mice/group.

Although [^{11}C]PK11195 has demonstrated utility in detecting microglial activation in HD patient studies, its poor brain permeability and high lipophilicity (leading to poor signal-to-background images and low sensitivity) has limited its widespread use (117). Recent studies have demonstrated the utility of second generation TSPO–PET tracers for detecting subtle neuroinflammation in cognitively normal National Football League athletes with a history of concussion (57) and in

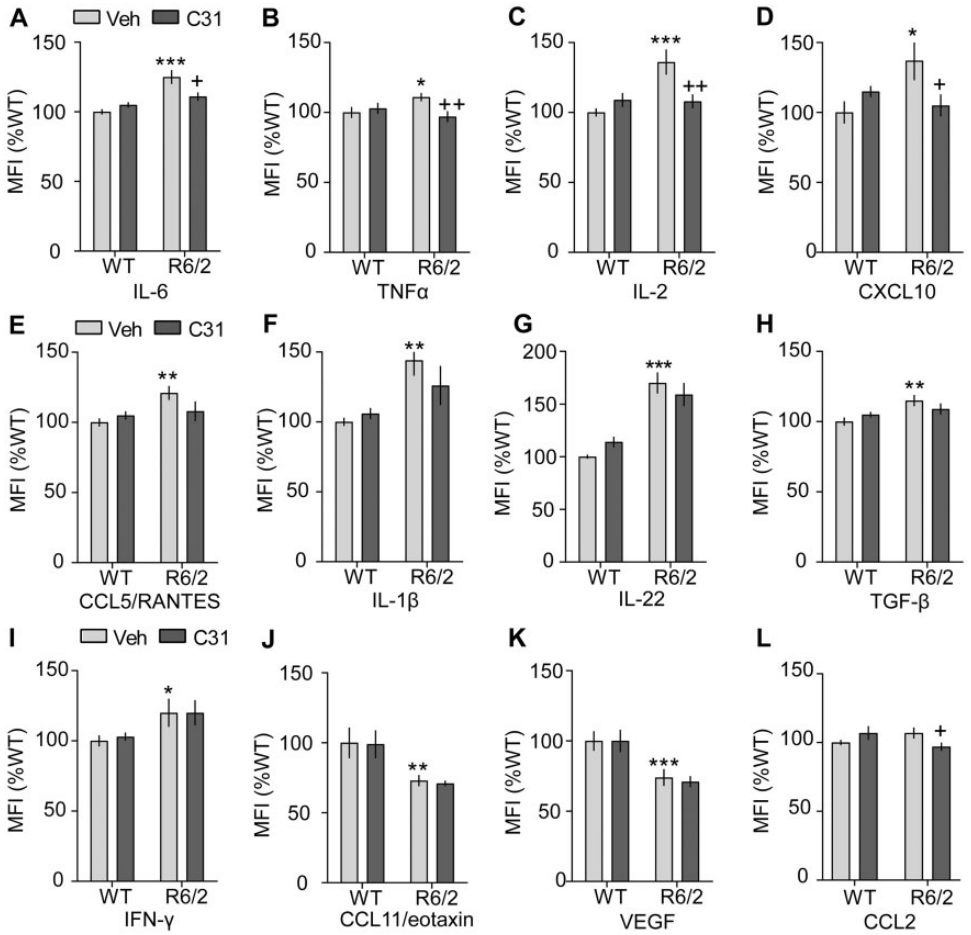

Figure 8. Effects of LM11A-31 on cytokine levels in the striatum of R6/2 mice. Relative cytokine concentrations in striatal lysates from 11- to 12-week-old WT and R6/2 mice treated with vehicle (Veh) or LM11A-31 (C31; $n = 5$–9 mice/group) were measured using an antibody-based 38-plex Luminex array. Quantification of cytokine levels that were significantly different between the genotypes or with C31 treatment are shown, including: interleukin (IL)-6 (**A**), tumor necrosis factor α (TNFα) (**B**), IL-2 (**C**), CXCL10 (**D**), chemokine (C-C motif) ligand 5 (CCL5)/regulated on activation normal T cell expressed and secreted (RANTES) (**E**), IL-1β (**F**), IL-22 (**G**), transforming growth factor β (TGF-β) (**H**), interferon-γ (IFN-γ) (**I**), CCL11/eotaxin (**J**), vascular endothelial growth factor (VEGF) (**K**) and CCL2 (**L**). For quantification of cytokine levels that did not show significant differences between the genotypes, see (Supplementary Material, Fig. 6). Results are expressed as the mean of the median fluorescence intensity (MFI) ± s.e.m. and normalized by the WT-Veh group of that Luminex assay. Statistical significance was determined with an ANOVA and Fisher's LSD or Student's *t*-test. $^{*}P < 0.05$, $^{**}P \leq 0.01$ and $^{***}P \leq 0.005$ versus WT-Veh; $^{+}P \leq 0.05$ and $^{++}P \leq 0.01$ versus R6/2-Veh.

prodromal Alzheimer's disease patients (118). [^{18}F]PBR06, used in the current study, is one of the second generation TSPO radiotracers with high brain bioavailability and increased sensitivity compared with [^{11}C]PK11195, and has been successfully translated for clinical use (48,49). Most second generation TSPO tracers display differing binding affinities (low, mixed, and high) in patients owing to the rs6971 polymorphism on the TSPO gene. This polymorphism does not exist in rodents, however when translating second generation tracers from preclinical to clinical studies, binding differences can be controlled for by excluding low-affinity binders and applying appropriate modeling/corrections to compare high- and mixed-affinity binders (62,119–121). Although the proportion of participants (i.e. low-affinity-binders) needing to be excluded from a TSPO–PET study using a second generation radiotracer is minimal, there has been a recent push to develop newer TSPO–PET tracers that are not sensitive to the rs6971 polymorphism (64). Importantly, even with these challenges, TSPO–PET remains the best characterized molecular imaging biomarker for microglial activation and continues to enhance our understanding of the *in vivo* anatomical distribution and temporal dynamics of inflammatory processes in living subjects with various diseases (120).

In addition to TSPO–PET imaging, other potential prognostic and/or disease state biomarkers have been identified, including additional molecular imaging markers, some of which have been shown to be effective in HD patients particularly via longitudinal programs such as TRACK-HD and PREDICT-HD (17–23). While these currently available measures have proven useful most have limitations primarily concerning longitudinal consistency and relevance to broad therapeutic applications. For instance, in HD patients, PET imaging for molecular markers of brain metabolism, phosphodiesterases, and the dopaminergic, cannabinoid and adrenergic systems have been used to detect disease state in premanifest and manifest stages although with varying degrees of sensitivity, reliability and applicability to broad therapeutics, if the goal is treatment monitoring (18). Current clinical biomarkers such as the Unified Huntington's Disease Rating Scale (UHDRS) for motor and cognitive performance have high functional significance to patients but suffer from variability and significantly limited sensitivity for

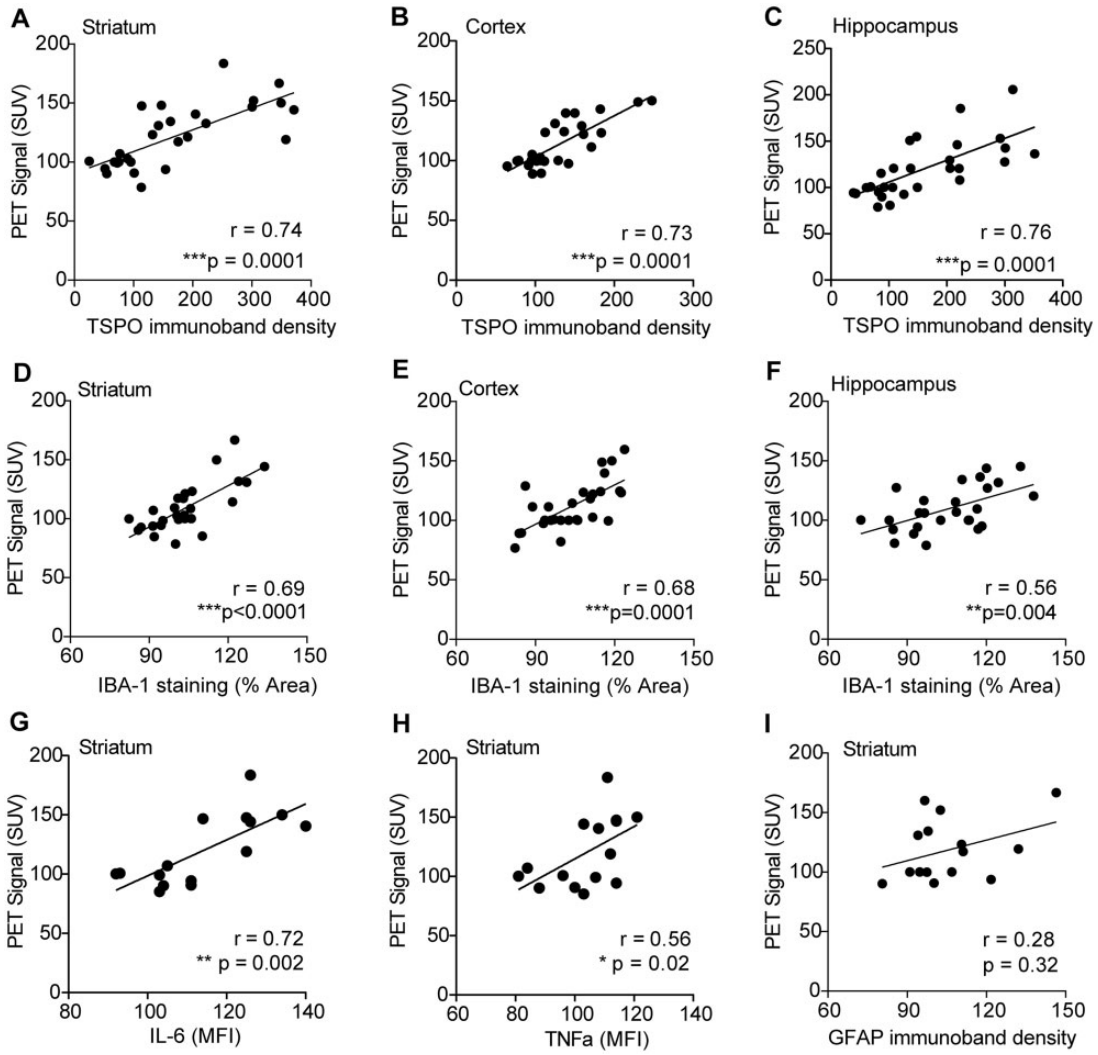

Figure 9. Correlations between [^{18}F]PBR06-PET uptake and levels of TSPO, IBA-1, cytokines and GFAP in R6/2 mice. Scatterplots with linear regression lines showing the associations between [^{18}F]PBR06-PET signal and TSPO immunoband density (**A–C**) and area (%) occupied by IBA-1 immunostaining (**D–F**) in striatum, cortex and hippocampus as well as cytokine levels (**G**, **H**) and GFAP immunoband density (**I**) in striatum ($n = 6$–10 mice/group, groups are combined for the analysis) of 11- to 12-week-old R6/2 mice. Spearman rank-order correlation coefficients (r) and P values are shown.

detecting disease state (19). Biochemical markers involving quantification of specific molecules in biofluids have the potential to measure indices of essential pathological processes but may be particular for a given therapeutic intervention (e.g. measuring huntingtin levels in CSF) (19,20,122). Recent advances in biochemical biomarker development identified neurofilament light chain protein (NfL) as a potential plasma biomarker with prognostic value for onset and progression in HD patients (17) and could be applicable for monitoring the efficacy of a wide-array of therapeutics as it is expunged from degenerating neurons. As mentioned above, plasma cytokine/chemokine levels show potential as HD biomarkers (43,107) and while the peripheral immune response may also be indicative of other non-HD-related comorbidities particularly in late-stage patients, it may be a useful biomarker in pre- and early-HD stages especially in conjunction with other biomarkers. In all, combining multiple biomarkers with particular advantages, such as the established UHDRS with biochemical biomarkers (e.g. plasma cytokine and NfL levels) and TSPO–PET neuroimaging with a second generation radiotracer (e.g. [^{18}F]PBR06) could be a viable and powerful option for clinical trials (19,123).

In conclusion, the results of this study are the first to indicate that TSPO–PET using [^{18}F]PBR06 enables sensitive detection of activated microglia in two HD mouse models and at multiple stages, including early disease progression. Moreover, these data show that [^{18}F]PBR06-PET imaging can be used as a measure of decreased neuroinflammation that accompanies LM11A-31 treatment. Thus, [^{18}F]PBR06-PET is a potential surrogate biomarker for monitoring disease progression and efficacy of LM11A-31 and other putative HD therapeutics that modulate neuroinflammation. Establishing neuroinflammatory biomarkers could have a broad beneficial impact on HD therapeutic development as numerous anti-inflammatory based therapies have been proposed for HD and many other treatments secondarily reduce/modulate neuroinflammation (124). A novelty and benefit of LM11A-31 is that it is currently in Phase IIa clinical testing for Alzheimer's disease, thus determining mouse-to-human translatable biomarkers that enable non-invasive

monitoring of therapeutic response will likely expedite the advancement of LM11A-31 to HD clinical testing.

Materials and Methods

Study design

This proof-of-concept study aimed to determine if TSPO–PET can be used as a translatable biomarker to monitor treatment response of putative HD therapeutics. This possibility was examined in two steps. First, we examined whether TSPO–PET imaging can detect microglial activation in HD mouse models as it does in HD patients (41–45). [^{18}F]PBR06 was the TSPO radiotracer employed since it has greater affinity and produces better signal-to-background images than [^{11}C]PK11195, which was used in the studies involving HD patients (41–45,48,50). If positive results were obtained in this initial study, our next step was designed to examine the feasibility of utilizing [^{18}F]PBR06-PET to monitor treatment response using the p75^{NTR} ligand LM11A-31 as a prototype since this compound was previously shown to reduce neuroinflammation in HD mice (7).

Our cross-sectional pilot studies assessing if [^{18}F]PBR06-PET detects genotype differences in activated microglia were conducted in late-symptomatic 11- to 12-week-old male R6/2 mice and their age- and gender-matched WT littermates. Cross-sectional studies were chosen for R6/2 mice because of the severity and rapid development of their disease symptoms which makes imaging these mice multiple times, particularly before treatment, very difficult because of their high mortality rate with excessive handling and the young age at which dosing starts (4 weeks of age). The R6/2 mouse model of HD was used as these mice rapidly and reliably develop robust HD symptoms and pathology, including activated microglia, as early as 4–6 weeks of age (33,65,83). Brain TSPO–PET/CT images were acquired as either a 60-min dynamic scan ($n = 3$–4 mice/group) started immediately after [^{18}F]PBR06 injection or a 10-min static scan started ~50 min later ($n = 5$–7 mice/group). MR imaging was performed ~1 week before PET scans on representative WT mice and all R6/2 mice so that resulting images could be co-registered with PET/CT scans to enable more precise delineation of pre-selected VOIs. Individual MR images are particularly important for R6/2 mice since marked brain volume loss, including striatum, is evident (7,65,80). If an MRI of a particular mouse had insufficient quality because of technical difficulties, an MRI of a weight- and genotype-matched mouse was used for analysis. [^{18}F]PBR06-PET detected genotype differences in activated microglia, so we went on to explore whether this method could also monitor therapeutic efficacy of LM11A-31.

A second cohort of male WT and R6/2 mice was used to investigate if [^{18}F]PBR06-PET could detect reductions in microglia activation associated with LM11A-31 treatment. A 2 ×2 [WT/transgenic×vehicle/LM11A-31] study design with random group assignment was used. LM11A-31 was administered to WT and R6/2 mice for ~7 weeks starting at 4 weeks of age until PET/CT imaging at ~11–12 weeks old. This treatment paradigm was used previously to demonstrate that LM11A-31 alleviates neuropathology, including microglial activation, and motor and cognitive deficits in R6/2 mice (7). Mice underwent either a 60-min dynamic scan ($n = 4$–5 mice/group) or a 10-min static scan started ~20 min after radiotracer injection ($n = 5$–8 mice/group). The 20- to 30-min interval after injection was chosen as the optimal acquisition time for the static scans based on time–radioactivity curves generated from dynamic recordings. This timeframe occurred after the radiotracer had cleared from the blood pool and it generated reproducible SUVs as it produced high signal-to-background ratios.

The effectiveness of [^{18}F]PBR06-PET in monitoring the reductive effects of LM11A-31 on microglial activation was also assessed in BACHD mice. These mice better represent the genetic component of HD and have a slower disease progression which is suitable for investigating/targeting early degenerative mechanisms (83). Male BACHD mice and age-matched WTs were imaged in two cohorts designed as cross-sectional studies to determine if [^{18}F]PBR06-PET could detect microglial activation and effects of LM11A-31 at 9 and/or 5 months of age, representing mid- and early-symptomatic stages, respectively. The first cohort of BACHD mice and their WT littermates were PET/CT imaged at 9 months of age, as we previously showed that microglia are activated in these mice at this age; earlier ages have not been investigated (7). Moreover, microglial activation and other key HD neuropathologies were reduced and motor and cognitive function were improved in 9-month-old BACHD mice treated with LM11A-31 compared with those given vehicle (7). These BACHD and WT mice were treated with vehicle or LM11A-31 (2×2 study design) for 7 months starting at 2 months of age. Mice received either a 60-min dynamic scan ($n = 6$–9 mice/group) or a 10-min static scan started ~20 min after [^{18}F]PBR06 injection ($n = 2$ mice/group). Mice from the static scans were not analyzed separately but combined with the appropriate timeframe from the dynamic scans and with the 9-month-old mice from BACHD Cohort 2 (total $n = 11$–14 mice/group). To replicate these results and to examine an earlier age, a second cohort of WT and BACHD mice treated with vehicle or LM11A-31 were PET/CT imaged at 5 and 9 months old. At 5 months of age, all mice received a dynamic scan ($n = 6$–8 mice/group) and at 9 months they received either a dynamic scan or a static scan started ~20 min after [^{18}F]PBR06 injection (total $n = 4$–6 mice/group). For both cohorts, MR imaging was performed 5–8 days before PET scans on representative WT and BACHD mice as these mice do not undergo brain volume loss at the age imaging was conducted (81).

After PET imaging, all mice were euthanized so that one brain hemisphere could be extracted for autoradiography or immunohistochemistry and the other for immunoblotting. The pre-selected VOIs used for histological and PET image analysis are the main brain areas undergoing degeneration in HD patients and mice, including R6/2 and BACHD (2,3,65,66). All dosing and quantitative analyses were conducted by experimenters that were blind to the treatment and genotype conditions. Group size required to obtain statistical significance on analyses of neuropathological endpoints was determined based on previously published studies using these mouse models (7,66,83,125).

Mice and genotyping

All animal procedures were conducted in accordance with the National Institutes of Health Guide for the Care and Use of Laboratory Animals using protocols approved by the Institutional Animal Care and Use Committee at Stanford University. These protocols included efforts to minimize animal suffering and numbers used. This study used both the R6/2 and BACHD mouse models of HD. Breeding pairs of R6/2 mice were purchased from Jackson Laboratories [female hemizygous ovarian transplant B6CBA-TgN (HD exon1)62; JAX stock

#006494]. Male R6/2 mice in this study had an average of 125 ± 3 (mean ± SD) CAG repeats. Male BACHD mice, and their WT littermates, were also purchased from Jackson (stock #008197). BACHD mice used in this study all had 98 CAG repeats. Mouse husbandry for both models involved group housing (3–5 mice/cage) with cotton nestlets and rodent chow *ad libitum*. Tail DNA was used for genotyping via real-time PCR by TransnetYX, Inc. (Cordova, TN, USA) and CAG repeat number measurement via ABI GeneMapper 4.0 by Laragen, Inc. (Los Angeles, CA, USA).

LM11A-31

LM11A-31 [2-amino-3-methyl-pentanoic acid (2-morpholin-4-yl-ethyl)-amide] is a water soluble isoleucine derivative identified via *in silico* screening for compounds corresponding to the nerve growth factor loop 1 β-turn domain that interacts with $p75^{NTR}$; chemical structure and pharmacokinetics/dynamics are detailed in previous publications (15,16,126,127). The sulfate salt form of LM11A-31 [(2S,3S)-2-amino-3-methyl-*N*-(2-morpholinoethyl) pentanamide] was used in this study (MW = 439.34; 50 mg of the salt contains 30 mg of the free base) and was custom manufactured by Ricerca Biosciences at >99% purity. This form of LM11A-31 successfully completed Phase I clinical trials evaluating safety and pharmacokinetics in healthy individuals and is currently in Phase IIa clinical trials for mild to moderate Alzheimer's disease (ClinicalTrials.gov: NCT03069014).

For both R6/2 and BACHD mice, LM11A-31 was dissolved in sterile water and administered to experimental groups after 4 h of fasting at 50 mg/kg (10 ml/kg) via oral gavage once daily 5–6 days/week and vehicle control groups received water in the same manner. This dose was shown previously to reduce HD-related pathology, including microglial activation, and improve motor and cognitive ability in both mouse models (7).

Small animal MR imaging

Five to eight days before PET imaging, MR imaging was performed using a small animal Varian Magnex Scientific scanner with 7.0 Tesla field strength and custom designed pulse sequences and radiofrequency coils. Mice were anesthetized with isoflurane gas (2–3% induction, 1.5–2% maintenance) and body temperature and respiration rate were monitored throughout the scan. Coronal brain images (0.7 mm slice) were acquired (~15–20 min) using T2-weighted fast spin echo sequences (TE/TR 58.5 ms/4000 ms), 9 NEX, a 256×256 matrix and 20×20 field of view.

Small animal PET/CT image acquisition and analysis

[^{18}F]PBR06 [*N*-(2,5-dimethoxybenzyl)-2-(18)F-fluoro-*N*-(2-phenoxyphenyl)acetamide] was synthesized via nucleophilic aliphatic substitution, as described previously (47,51,61,128) with a non-decay corrected radiochemical yield of 1.95 ± 0.32% and a specific radioactivity of 120.5 ± 14.3 GBq/μmol at the end of bombardment (n = 10; mean ± S.E.M.). Mice were anesthetized with isoflurane gas (2–3% induction, 1.5–2% maintenance) and a catheter with 27 g needle and PU tubing (SAI infusion Technologies) was inserted into their tail veins. For dynamic PET/CT scans, four mice (one mouse/treatment group unless technical issues occurred) were concurrently placed into a microPET/CT hybrid scanner (Inveon, Siemens) and CT images were acquired (~10 min) to provide an anatomical reference frame for the corresponding PET data. PET scans (60 min) acquired in list mode format were started just before investigators synchronously injected all mice with [^{18}F]PBR06 (7.5–9.5 MBq) intravenously (i.v.) via the catheter (followed by a 50 μl saline flush). For dynamic pre-blocking studies, PK11195 (1 mg/kg) was injected 10 min before [^{18}F]PBR06 injection. Static PET scans (10 min) were conducted the same way as dynamic scans except that after [^{18}F]PBR06 injection PET/CT acquisition was started ~20 or 50 min later.

PET data were sorted into 0.5 mm sinogram bins and 19 time frames (4×15 s, 4×60 s, 11×300 s) and images were reconstructed with 2 iterations of a 3-Dimensional Ordered Subsets Expectation Maximization algorithm (12 subsets) and 18 iterations of the accelerated version of 3D-map (matrix size 128×128×159). Reconstructed PET images were co-registered with CT and MRI images using Inveon Research Workplace image analysis software version 4.0 (Siemens) and radioactivity concentrations were obtained by drawing 3D regions around whole brain and VOIs in predefined brain regions (Supplementary Material, Fig. S7). VOIs (mean volume ± S.E.M.) included striatum (rostral to mid-caudal levels; 7.4 ± 0.2 mm^3), the somatosensory 1 and motor cortices (8.3 ± 0.2 mm^3), dorsal hippocampus (2.3 ± 0.1 mm^3), rostral/dorsal thalamus (5.2 ± 0.2 mm^3) and rostral hypothalamus (at the levels of the medial preoptic area and anterior hypothalamic area; 1.9 ± 0.1 mm^3). Percent injected dose per gram (%ID/g) was calculated for each VOI using the decay corrected dose at the time of the scan. SUVs were also computed using the following equation: SUV = [radioactivity per milliliter tissue (nCi/cc)]/[(injected radioactivity decay corrected to the injection time/body weight (g)]. SUVs were also normalized to the WT-Veh group of the yoked PET scan to minimize variability between imaging sessions.

Plasma free fraction (f_P)

To measure f_p of [^{18}F]PBR06, blood samples were drawn via cardiac puncture from 9-month-old BACHD mice used for static PET scans and processed according to previously described methods (47,129). Briefly, after blood samples were centrifuged, plasma was collected and whole plasma radioactivity measured with a gamma counter. Next, plasma samples were loaded onto an ultrafiltration device and centrifuged at 1000*g* for 30 min at room temperature. Ultrafiltrate was counted with a gamma counter and, after decay correction, the f_p was calculated.

Ex vivo autoradiography

Following their final static PET scan, a subset of mice from each mouse model (n = 3–6 mice/group/model) was transcardially perfused with saline, their brains were embedded in OCT, and coronal sections (20 μm) were cut on a cryostat. Autoradiography was performed, as described previously (47,130), and anatomy was confirmed by standard Nissl staining (131). For quantification of autoradiography images, five sections per mouse were analyzed, and radiotracer uptake was assessed using VOIs that correspond to brain regions used for PET image analysis. Mean signal intensity values per area of each VOI were obtained and SUVs were computed and normalized to the WT-vehicle mouse on that autoradiography film.

Western immunoblotting

After PET/CT imaging, mice from each mouse model were transcardially perfused with saline and then striatum, hippocampus

and cortex were dissected from one brain hemisphere and flash frozen at −80°C. The other brain hemisphere was used for immunostaining (see below). Preparation of tissue homogenates was conducted, as described previously (66), briefly, tissue was sonicated in RIPA lysis buffer containing protease and phosphatase inhibitors. Lysates from each genotype and treatment group were electrophoresed through NuPAGE 4–12% Bis–Tris gel with MES SDS running buffer (Invitrogen) and transferred to polyvinylidene difluoride membranes (Immobilon-FL, Millpore). Membranes were probed using an antibody to TSPO (PBR; AbCam; #ab109497) or GFAP (DAKO; #z0334) and α-tubulin monoclonal antibody (Sigma, #T6074) as a loading control. Secondary antibodies were IRDye® 800CW and IRDye® 680RD and imaged with an Odyssey® CLx near-infrared fluorescence imaging system (Li-Cor Biosciences) or with enhanced chemiluminescence detection system (GE Healthcare). Immunoreactive bands were manually outlined and densities were measured using Image Studio Lite software (Li-Cor Biosciences) or Un-Scan-It gel software (v6.1, Silk Scientific). The densities of immunoreactive bands were expressed as a fraction of tubulin in the same lane. Samples were run two to four separate times per mouse and data was normalized to the WT-Veh group of that gel then averaged. In the western blot figures, some non-adjacent bands from the same gel were moved together for comparison purposes; these were separated by thin black lines.

Measuring striatal cytokine levels

The relative concentrations of cytokines were measured using the antibody-based 38-plex Luminex array, according to kit instructions (Affymetrix), in the Stanford Human Immune Monitoring Center. Briefly, striatal lysates from WT and R6/2 mice prepared for western blotting (measured in duplicate) were incubated in 96-well plates containing mixed antibody-linked beads and custom assay control beads (Radix Biosolutions). Plates were incubated in biotinylated detection antibody, then streptavidin-PE, and finally reading buffer. Plates were read (Luminex 200) with a lower bound of 50 beads/sample per cytokine. The assay was performed in two sets so quantifications for each mouse were normalized to the WT-vehicle group of the yoked set.

Immunostaining

The brain hemisphere that was not used for Western immunoblotting was immersion-fixed overnight in 4% paraformaldehyde in 0.1 M phosphate buffer (PB; pH 7.4), cryoprotected in 30% sucrose/PB and sectioned (40 μm, coronal) using a freezing microtome. Free-floating sections were processed for IBA-1 (WAKO; #019-19741) immunostaining to assess activated microglia using procedures described previously (7,66). IBA-1 immunostaining was analyzed in two to three sections per brain area per mouse [8–12 sample fields (250×250 μm) per brain area]. Brain areas examined were striatum at rostral to mid-caudal levels (+1.34 to +0.02 mm relative to Bregma) (131), the somatosensory 1/motor cortices (+1.18 to −0.10 mm), and dorsal hippocampus (−1.58 to −2.3 mm) and closely adhered to the areas analyzed for PET signal. Sections were imaged at 20× and analyzed with Image J (v1.49p) subtract background and auto-threshold commands. Images were acquired with a Zeiss AxioImager M2 microscope, AxioCam Hrc camera and Neurolucida v11.07 (MBF) image analysis software. Immunostaining was performed in multiple sets, so quantifications for each mouse were normalized to the WT-vehicle group of that staining set.

Statistics

Statistical significance was determined using GraphPad Prism v6 software via a one-way analysis of variance with a Fisher's LSD *post hoc* test, a two-tailed Student's *t*-test for paired comparisons, and/or a non-parametric two-tailed Mann–Whitney *U* test if a Gaussian distribution could not be assumed. Values that were two standard deviations from the mean (criteria determined *a priori*) were removed as statistical outliers. Associations between [^{18}F]PBR06-PET signal and levels of TSPO, IBA-1 and cytokines were evaluated by calculating Spearman rank-order correlation coefficients (*r*) using GraphPad Prism v6. Results are expressed as group mean ± standard error of the mean (S.E.M.) and statistical significance was set at $P \leq 0.05$.

Supplementary Material

Supplementary Material is available at *HMG* online.

Acknowledgements

The authors would like to thank members of the Small Animal Imaging Facility at Stanford University, namely Dr Timothy Doyle for helping with the PET/CT imaging, Dr Laura Pisani for assisting with the MRIs and Dr Frezghi Habte for guidance on PET image analysis. We would also like to thank members of the Department of Radiology, Molecular Imaging Program at Stanford including Natasha Arskey and Bin Shen for assistance with [^{18}F]PBR06 radiosynthesis and Steven Machtaler and Shawn Scatliffe for their help with tail vein catheter insertion. Finally, we would like to acknowledge Yael Rosenberg-Hasson in the Stanford Human Immune Monitoring Center for performing the Luminex assay to measure cytokine levels.

Conflict of Interest statement. F.M.L. is listed as an inventor on patents relating to LM11A-31 which are assigned to the University of North Carolina, University of California (UC), San Francisco and the Department of Veterans Affairs (VA). F.M.L. is entitled to royalties distributed by the UC and VA per standard agreements. F.M.L. is a principal of, and has financial interest in PharmatrophiX, a company focused on the development of small molecule ligands for neurotrophin receptors that has licensed several of these patents. None of the other authors have competing interests.

Funding

This work was supported by the National Institutes of Health [R21 NS081089-01 to F.M.L.]; National Institute of Mental Health for their support with [^{18}F]PBR06 to F.T.C.; Taube Philanthropies to F.M.L; Koret Foundation [12-0160 to F.M.L.], and Wilma Marvelle Jones Huntington Disease Research Fund and Jean Perkins Foundation to F.M.L. The funding sources were not involved in any aspect of the study including, design, conduct, or submission. The research was designed by D.A.S., M.L.J., F.T.C. and F.M.L. and performed by D.A.S, M.L.J., N.P.B, S.S., C.C., J.K., A.S. and B.S. Data were analyzed by D.A.S., N.P.B., M.L.J. and S.S. Resources were provided by F.T.C. The manuscript was written

by D.A.S. and critically revised by M.L.J. and F.M.L. Funding to pay the Open Access publication charges for this article was provided by Taube Philanthropies and the Koret Foundation.

References

1. MacDonald, M. (1993) A novel gene containing a trinucleotide repeat that is expanded and unstable on Huntington's disease chromosomes. The Huntington's Disease Collaborative Research Group. *Cell*, **72**, 971–983.
2. Vonsattel, J. and DiFiglia, M. (1998) Huntington disease. *J. Neuropathol. Exp. Neurol.*, **57**, 369–384.
3. Vonsattel, J., Myers, R., Stevens, T., Ferrante, R., Bird, E. and Richardson, E.J. (1985) Neuropathological classification of Huntington's disease. *J. Neuropathol. Exp. Neurol.*, **44**, 559–577.
4. Walker, F.O. (2007) Huntington's disease. *Lancet*, **369**, 218–228.
5. Brito, V., Giralt, A., Enriquez-Barreto, L., Puigdellívol, M., Suelves, N., Zamora-Moratalla, A., Ballesteros, J.J., Martín, E.D., Dominguez-Iturza, N., Morales, M., Alberch, J. and Ginés, S. (2014) Neurotrophin receptor p75(NTR) mediates Huntington's disease-associated synaptic and memory dysfunction. *J. Clin. Invest.*, **124**, 4411–4428.
6. Plotkin, J.L., Day, M., Peterson, J.D., Xie, Z., Kress, G.J., Rafalovich, I., Kondapalli, J., Gertler, T.S., Flajolet, M., Greengard, P. *et al.* (2014) Impaired TrkB receptor signaling underlies corticostriatal dysfunction in Huntington's disease. *Neuron*, **83**, 178–188.
7. Simmons, D.A., Belichenko, N.P., Ford, E.C., Semaan, S., Monbureau, M., Aiyaswamy, S., Holman, C.M., Condon, C., Shamloo, M. and Massa, S.M. (2016) A small molecule $p75^{NTR}$ ligand normalizes signalling and reduces Huntington's disease phenotypes in R6/2 and BACHD mice. *Hum. Mol. Genet.*, **25**, 4920–4938.
8. Zuccato, C. and Cattaneo, E. (2007) Role of brain-derived neurotrophic factor in Huntington's disease. *Prog. Neurobiol.*, **81**, 294–330.
9. Zuccato, C., Valenza, M. and Cattaneo, E. (2010) Molecular mechanisms and potential therapeutical targets in Huntington's disease. *Physiol. Rev.*, **90**, 905–981.
10. Simmons, D.A. (2017) Modulating neurotrophin receptor signaling as a therapeutic strategy for Huntington's disease. *J. Huntington's Dis.*, **6**, 303–325.
11. Brito, V., Puigdellivol, M., Giralt, A., Del Toro, D., Alberch, J. and Gines, S. (2013) Imbalance of p75(NTR)/TrkB protein expression in Huntington's disease: implication for neuroprotective therapies. *Cell Death Dis.*, **4**, e595.
12. Miguez, A., Garcia-Diaz Barriga, G., Brito, V., Straccia, M., Giralt, A., Gines, S., Canals, J.M. and Alberch, J. (2015) Fingolimod (FTY720) enhances hippocampal synaptic plasticity and memory in Huntington's disease by preventing p75NTR up-regulation and astrocyte-mediated inflammation. *Hum. Mol. Genet.*, **24**, 4958–4970.
13. Ma, Q., Yang, J., Li, T., Milner, T.A. and Hempstead, B.L. (2015) Selective reduction of striatal mature BDNF without induction of proBDNF in the zQ175 mouse model of Huntington's disease. *Neurobiol. Dis.*, **82**, 466–477.
14. Zuccato, C., Marullo, M., Conforti, P., MacDonald, M.E., Tartari, M. and Cattaneo, E. (2007) Systematic assessment of BDNF and its receptor levels in human cortices affected by Huntington's disease. *Brain Pathol.*, **18**, 225–238.
15. Massa, S.M., Xie, Y., Yang, T., Harrington, A.W., Kim, M.L., Yoon, S.O., Kraemer, R., Moore, L.A., Hempstead, B.L. and Longo, F.M. (2006) Small, nonpeptide p75NTR ligands induce survival signaling and inhibit proNGF-induced death. *J. Neurosci.*, **26**, 5288–5300.
16. Yang, T., Knowles, J.K., Lu, Q., Zhang, H., Arancio, O., Moore, L.A., Chang, T., Wang, Q., Andreasson, K. and Rajadas, J. (2008) Small molecule, non-peptide p75 ligands inhibit Abeta-induced neurodegeneration and synaptic impairment. *PLoS One*, **3**, e3604.
17. Byrne, L.M., Rodrigues, F.B., Blennow, K., Durr, A., Leavitt, B.R., Roos, R.A.C., Scahill, R.I., Tabrizi, S.J., Zetterberg, H. and Langbehn, D. (2017) Neurofilament light protein in blood as a potential biomarker of neurodegeneration in Huntington's disease: a retrospective cohort analysis. *Lancet Neurol.*, **16**, 601–609.
18. Wilson, H., De Micco, R., Niccolini, F. and Politis, M. (2017) Molecular imaging markers to track Huntington's disease pathology. *Front. Neurol.*, **8**, 11.
19. Andre, R., Scahill, R.I., Haider, S. and Tabrizi, S.J. (2014) Biomarker development for Huntington's disease. *Drug Discov. Today*, **19**, 972–979.
20. Weir, D.W., Sturrock, A. and Leavitt, B.R. (2011) Development of biomarkers for Huntington's disease. *Lancet Neurol.*, **10**, 573–590.
21. Tabrizi, S.J., Scahill, R.I., Owen, G., Durr, A., Leavitt, B.R., Roos, R.A., Borowsky, B., Landwehrmeyer, B., Frost, C. and Johnson, H. (2013) Predictors of phenotypic progression and disease onset in premanifest and early-stage Huntington's disease in the TRACK-HD study: analysis of 36-month observational data. *Lancet Neurol.*, **12**, 637–649.
22. Ross, C.A., Aylward, E.H., Wild, E.J., Langbehn, D.R., Long, J.D., Warner, J.H., Scahill, R.I., Leavitt, B.R., Stout, J.C., Paulsen, J.S. *et al.* (2014) Huntington disease: natural history, biomarkers and prospects for therapeutics. *Nat. Rev. Neurol.*, **10**, 204–216.
23. Pagano, G., Niccolini, F. and Politis, M. (2016) Current status of PET imaging in Huntington's disease. *Eur. J. Nucl. Med. Mol. Imaging*, **43**, 1171–1182.
24. Tippett, L.J., Waldvogel, H.J., Snell, R.G., Vonsattel, J.P., Young, A.B. and Faull, R.L.M. (2017) The complexity of clinical Huntington's disease: developments in molecular genetics, neuropathology and neuroimaging biomarkers. *Adv. Neurobiol.*, **15**, 129–161.
25. Disatnik, M.H., Joshi, A.U., Saw, N.L., Shamloo, M., Leavitt, B.R., Qi, X. and Mochly-Rosen, D. (2016) Potential biomarkers to follow the progression and treatment response of Huntington's disease. *J. Exp. Med.*, **213**, 2655–2669.
26. Cosenza-Nashat, M., Zhao, M.L., Suh, H.S., Morgan, J., Natividad, R., Morgello, S. and Lee, S.C. (2009) Expression of the translocator protein of 18 kDa by microglia, macrophages and astrocytes based on immunohistochemical localization in abnormal human brain. *Neuropathol. Appl. Neurobiol.*, **35**, 306–328.
27. Veiga, S., Carrero, P., Pernia, O., Azcoitia, I. and Garcia-Segura, L.M. (2007) Translocator protein 18 kDa is involved in the regulation of reactive gliosis. *Glia*, **55**, 1426–1436.
28. Venneti, S., Lopresti, B.J. and Wiley, C.A. (2006) The peripheral benzodiazepine receptor (Translocator protein 18kDa) in microglia: from pathology to imaging. *Prog. Neurobiol.*, **80**, 308–322.
29. Banati, R.B. (2002) Visualising microglial activation in vivo. *Glia*, **40**, 206–217.
30. Meßmer, K. and Reynolds, G.P. (1998) Increased peripheral benzodiazepine binding sites in the brain of patients with Huntington's disease. *Neurosci. Lett.*, **241**, 53–56.

31. Chen, M.K. and Guilarte, T.R. (2008) Translocator protein 18 kDa (TSPO): molecular sensor of brain injury and repair. *Pharmacol. Ther.*, **118**, 1–17.
32. Dupont, A.C., Largeau, B., Santiago Ribeiro, M.J., Guilloteau, D., Tronel, C. and Arlicot, N. (2017) Translocator protein-18 kDa (TSPO) positron emission tomography (PET) imaging and its clinical impact in neurodegenerative diseases. *Int. J. Mol. Sci.*, **18**, 785.
33. Simmons, D.A., Casale, M., Alcon, B., Pham, N., Narayan, N. and Lynch, G. (2007) Ferritin accumulation in dystrophic microglia is an early event in the development of Huntington's disease. *Glia*, **55**, 1074–1084.
34. Crotti, A. and Glass, C.K. (2015) The choreography of neuroinflammation in Huntington's disease. *Trends Immunol.*, **36**, 364–373.
35. Ellrichmann, G., Reick, C., Saft, C. and Linker, R.A. (2013) The role of the immune system in Huntington's disease. *Clin. Dev. Immunol.*, **2013**, 541259.
36. Franciosi, S., Ryu, J.K., Shim, Y., Hill, A., Connolly, C., Hayden, M.R., McLarnon, J.G. and Leavitt, B.R. (2012) Age-dependent neurovascular abnormalities and altered microglial morphology in the YAC128 mouse model of Huntington disease. *Neurobiol. Dis.*, **45**, 438–449.
37. Sapp, E., Kegel, K., Aronin, N., Hashikawa, T., Uchiyama, Y., Tohyama, K., Bhide, P., Vonsattel, J. and DiFiglia, M. (2001) Early and progressive accumulation of reactive microglia in the Huntington disease brain. *J. Neuropathol. Exp. Neurol.*, **60**, 161–172.
38. Singhrao, S.K., Neal, J.W., Morgan, B.P. and Gasque, P. (1999) Increased complement biosynthesis by microglia and complement activation on neurons in Huntington's disease. *Exp. Neurol.*, **159**, 362–376.
39. Yang, H.M., Yang, S., Huang, S.S., Tang, B.S. and Guo, J.F. (2017) Microglial activation in the pathogenesis of Huntington's disease. *Front. Aging Neurosci.*, **9**, 193.
40. Moller, T. (2010) Neuroinflammation in Huntington's disease. *J. Neural. Transm.*, **117**, 1001–1008.
41. Politis, M., Pavese, N., Tai, Y.F., Tabrizi, S.J., Barker, R.A. and Piccini, P. (2008) Hypothalamic involvement in Huntington's disease: an in vivo PET study. *Brain*, **131**, 2860–2869.
42. Pavese, N., Gerhard, A., Tai, Y.F., Ho, A.K., Turkheimer, F., Barker, R.A., Brooks, D.J. and Piccini, P. (2006) Microglial activation correlates with severity in Huntington disease: a clinical and PET study. *Neurology*, **66**, 1638–1643.
43. Politis, M., Lahiri, N., Niccolini, F., Su, P., Wu, K., Giannetti, P., Scahill, R.I., Turkheimer, F.E., Tabrizi, S.J. and Piccini, P. (2015) Increased central microglial activation associated with peripheral cytokine levels in premanifest Huntington's disease gene carriers. *Neurobiol. Dis*, **83**, 115–121.
44. Politis, M., Pavese, N., Tai, Y.F., Kiferle, L., Mason, S.L., Brooks, D.J., Tabrizi, S.J., Barker, R.A. and Piccini, P. (2011) Microglial activation in regions related to cognitive function predicts disease onset in Huntington's disease: a multimodal imaging study. *Hum. Brain Mapp.*, **32**, 258–270.
45. Tai, Y.F., Pavese, N., Gerhard, A., Tabrizi, S.J., Barker, R.A., Brooks, D.J. and Piccini, P. (2007) Microglial activation in presymptomatic Huntington's disease gene carriers. *Brain*, **130**, 1759–1766.
46. Tai, Y.F., Pavese, N., Gerhard, A., Tabrizi, S.J., Barker, R.A., Brooks, D.J. and Piccini, P. (2007) Imaging microglial activation in Huntington's disease. *Brain Res. Bull.*, **72**, 148–151.
47. James, M.L., Belichenko, N.P., Nguyen, T.-V.V., Andrews, L.E., Ding, Z., Liu, H., Bodapati, D., Arksey, N., Shen, B., Cheng, Z. *et al.* (2015) PET imaging of translocator protein (18 kDa) in a mouse model of Alzheimer's disease using N-(2,5-dimethoxybenzyl)-2-18F-fluoro-N-(2-phenoxyphenyl) acetamide. *J. Nucl. Med.*, **56**, 311–316.
48. Fujimura, Y., Kimura, Y., Simeon, F.G., Dickstein, L.P., Pike, V.W., Innis, R.B. and Fujita, M. (2010) Biodistribution and radiation dosimetry in humans of a new PET ligand, (18)F-PBR06, to image translocator protein (18 kDa). *J. Nucl. Med.*, **51**, 145–149.
49. Fujimura, Y., Zoghbi, S.S., Simeon, F.G., Taku, A., Pike, V.W., Innis, R.B. and Fujita, M. (2009) Quantification of translocator protein (18 kDa) in the human brain with PET and a novel radioligand, (18)F-PBR06. *J. Nucl. Med.*, **50**, 1047–1053.
50. Imaizumi, M., Briard, E., Zoghbi, S.S., Gourley, J.P., Hong, J., Musachio, J.L., Gladding, R., Pike, V.W., Innis, R.B. and Fujita, M. (2007) Kinetic evaluation in nonhuman primates of two new PET ligands for peripheral benzodiazepine receptors in brain. *Synapse*, **61**, 595–605.
51. Briard, E., Zoghbi, S.S., Siméon, F.G., Imaizumi, M., Gourley, J.P., Shetty, H.U., Lu, S., Fujita, M.., Innis, R.B. and Pike, V.W. (2009) Single-step high-yield radiosynthesis and evaluation of a sensitive 18F-labeled ligand for imaging brain peripheral benzodiazepine receptors with PET. *J. Med. Chem.*, **52**, 688–699.
52. Kreisl, W.C., Lyoo, C.H., Liow, J.-S., Wei, M., Snow, J., Page, E., Jenko, K.J., Morse, C.L., Zoghbi, S.S., Pike, V.W., Turner, R.S. and Innis, R.B. (2016) (11)C-PBR28 binding to translocator protein increases with progression of Alzheimer's disease. *Neurobiol. Aging*, **44**, 53–61.
53. Wang, L., Cheng, R., Fujinaga, M., Yang, J., Zhang, Y., Hatori, A., Kumata, K., Yang, J., Vasdev, N., Du, Y. *et al.* (2017) A facile radiolabeling of [18F]FDPA via spirocyclic iodonium ylides: preliminary PET imaging studies in preclinical models of neuroinflammation. *J. Med. Chem.*, **60**, 5222–5227.
54. Endres, C.J., Pomper, M.G., James, M., Uzuner, O., Hammoud, D.A., Watkins, C.C., Reynolds, A., Hilton, J., Dannals, R.F. and Kassiou, M. (2009) Initial evaluation of 11C-DPA-713, a novel TSPO PET ligand, in humans. *J. Nucl. Med.*, **50**, 1276–1282.
55. James, M.L., Fulton, R.R., Henderson, D.J., Eberl, S., Meikle, S.R., Thomson, S., Allan, R.D., Dolle, F., Fulham, M.J. and Kassiou, M. (2005) Synthesis and in vivo evaluation of a novel peripheral benzodiazepine receptor PET radioligand. *Bioorganic Med. Chem.*, **13**, 6188–6194.
56. Boutin, H., Chauveau, F., Thominiaux, C., Gregoire, M.C., James, M.L., Trebossen, R., Hantraye, P., Dolle, F., Tavitian, B. and Kassiou, M. (2007) 11C-DPA-713: a novel peripheral benzodiazepine receptor PET ligand for in vivo imaging of neuroinflammation. *J. Nucl. Med.*, **48**, 573–581.
57. Coughlin, J.M., Wang, Y., Minn, I., Bienko, N., Ambinder, E.B., Xu, X., Peters, M.E., Dougherty, J.W., Vranesic, M., Koo, S.M. *et al.* (2017) Imaging of glial cell activation and white matter integrity in brains of active and recently retired national football league players. *JAMA Neurol.*, **74**, 67–74.
58. James, M.L., Fulton, R.R., Vercoullie, J., Henderson, D.J., Garreau, L., Chalon, S., Dolle, F., Selleri, S., Guilloteau, D. and Kassiou, M. (2008) DPA-714, a new translocator protein-specific ligand: synthesis, radiofluorination, and pharmacologic characterization. *J. Nucl. Med.*, **49**, 814–822.
59. Mizrahi, R., Rusjan, P.M., Kennedy, J., Pollock, B., Mulsant, B., Suridjan, I., De Luca, V., Wilson, A.A. and Houle, S. (2012) Translocator protein (18 kDa) polymorphism (rs6971)

explains in-vivo brain binding affinity of the PET radioligand [(18)F]-FEPPA. *J. Cereb. Blood Flow Metab.*, **32**, 968–972.
60. Boutin, H., Murray, K., Pradillo, J., Maroy, R., Smigova, A., Gerhard, A., Jones, P.A. and Trigg, W. (2015) ^{18}F-GE-180: a novel TSPO radiotracer compared to 11C-R-PK11195 in a preclinical model of stroke. *Eur. J. Nucl. Med. Mol. Imaging*, **42**, 503–511.
61. Wadsworth, H., Jones, P.A., Chau, W.F., Durrant, C., Fouladi, N., Passmore, J., O'Shea, D., Wynn, D., Morisson-Iveson, V. and Ewan, A. (2012) [(1)(8)F]GE-180: a novel fluorine-18 labelled PET tracer for imaging Translocator protein 18 kDa (TSPO). *Bioorganic Med. Chem. Lett.*, **22**, 1308–1313.
62. Fan, Z., Calsolaro, V., Atkinson, R.A., Femminella, G.D., Waldman, A., Buckley, C., Trigg, W., Brooks, D.J., Hinz, R. and Edison, P. (2016) Flutriciclamide (18F-GE180) PET: first-in-human PET study of novel third generation in vivo marker of human translator protein. *J. Nucl. Med.*, **57**, 1753–1759.
63. Fujita, M., Kobayashi, M., Ikawa, M., Gunn, R.N., Rabiner, E.A., Owen, D.R., Zoghbi, S.S., Haskali, M.B., Telu, S., Pike, V.W. *et al.* (2017) Comparison of four 11C-labeled PET ligands to quantify translocator protein 18 kDa (TSPO) in human brain: (R)-PK11195, PBR28, DPA-713, and ER176-based on recent publications that measured specific-to-non-displaceable ratios. *EJNMMI Res.*, **7**, 84.
64. Ikawa, M., Lohith, T.G., Shrestha, S., Telu, S., Zoghbi, S.S., Castellano, S., Taliani, S., Da Settimo, F., Fujita, M., Pike, V.W. *et al.* (2017) 11C-ER176, a radioligand for 18-kDa translocator protein, Has adequate sensitivity to robustly image all three affinity genotypes in human brain. *J. Nucl. Med.*, **58**, 320–325.
65. Mangiarini, L., Sathasivam, K., Seller, M., Cozens, B., Harper, A., Hetherington, C., Lawton, M., Trottier, Y., Lehrach, H., Davies, S. *et al.* (1996) Exon 1 of the HD gene with an expanded CAG repeat is sufficient to cause a progressive neurological phenotype in transgenic mice. *Cell*, **87**, 493–506.
66. Simmons, D.A., Belichenko, N.P., Yang, T., Condon, C., Monbureau, M., Shamloo, M., Jing, D., Massa, S.M. and Longo, F.M. (2013) A small molecule TrkB ligand reduces motor impairment and neuropathology in R6/2 and BACHD mouse models of Huntington's disease. *J. Neurosci.*, **33**, 18712–18727.
67. Wacker, J.L., Huang, S.Y., Steele, A.D., Aron, R., Lotz, G.P., Nguyen, Q., Giorgini, F., Roberson, E.D., Lindquist, S., Masliah, E. *et al.* (2009) Loss of Hsp70 exacerbates pathogenesis but not levels of fibrillar aggregates in a mouse model of Huntington's disease. *J. Neurosci.*, **29**, 9104–9114.
68. Vicidomini, C., Panico, M., Greco, A., Gargiulo, S., Coda, A.R., Zannetti, A., Gramanzini, M., Roviello, G.N., Quarantelli, M., Alfano, B. *et al.* (2015) In vivo imaging and characterization of [(18)F]DPA-714, a potential new TSPO ligand, in mouse brain and peripheral tissues using small-animal PET. *Nucl. Med. Biol.*, **42**, 309–316.
69. Liu, B., Le, K.X., Park, M.A., Wang, S., Belanger, A.P., Dubey, S., Frost, J.L., Holton, P., Reiser, V., Jones, P.A. *et al.* (2015) In vivo detection of age- and disease-related increases in neuroinflammation by 18F-GE180 TSPO MicroPET imaging in wild-type and Alzheimer's transgenic mice. *J. Neurosci.*, **35**, 15716–15730.
70. Antkiewicz-Michaluk, L., Mukhin, A.G., Guidotti, A. and Krueger, K.E. (1988) Purification and characterization of a protein associated with peripheral-type benzodiazepine binding sites. *J. Biol. Chem.*, **263**, 17317–17321.
71. Phan, J., Hickey, M.A., Zhang, P., Chesselet, M.F. and Reue, K. (2009) Adipose tissue dysfunction tracks disease progression in two Huntington's disease mouse models. *Hum. Mol. Genet.*, **18**, 1006–1016.
72. Fain, J.N., Del Mar, N.A., Meade, C.A., Reiner, A. and Goldowitz, D. (2001) Abnormalities in the functioning of adipocytes from R6/2 mice that are transgenic for the Huntington's disease mutation. *Hum. Mol. Genet.*, **10**, 145–152.
73. Logan, J. (2000) Graphical analysis of PET data applied to reversible and irreversible tracers. *Nucl. Med. Biol.*, **27**, 661–670.
74. Zanotti-Fregonara, P., Chen, K., Liow, J.S., Fujita, M. and Innis, R.B. (2011) Image-derived input function for brain PET studies: many challenges and few opportunities. *J. Cereb. Blood Flow Metab.*, **31**, 1986–1998.
75. James, M.L., Belichenko, N.P., Shuhendler, A.J., Hoehne, A., Andrews, L.E., Condon, C., Nguyen, T.V., Reiser, V., Jones, P., Trigg, W. *et al.* (2017) [18F]GE-180 PET detects reduced microglia activation after LM11A-31 therapy in a mouse model of Alzheimer's disease. *Theranostics*, **7**, 1422–1436.
76. Yamasaki, T., Fujinaga, M., Yui, J., Ikoma, Y., Hatori, A., Xie, L., Wakizaka, H., Kumata, K., Nengaki, N., Kawamura, K. *et al.* (2014) Noninvasive quantification of metabotropic glutamate receptor type 1 with [(1)(1)C]ITDM: a small-animal PET study. *J. Cereb. Blood Flow Metab*, **34**, 606–612.
77. Nair, A., Veronese, M., Xu, X., Curtis, C., Turkheimer, F., Howard, R. and Reeves, S. (2016) Test–retest analysis of a non-invasive method of quantifying [(11)C]-PBR28 binding in Alzheimer's disease. *EJNMMI Res.*, **6**, 72.
78. Kinahan, P.E. and Fletcher, J.W. (2010) Positron emission tomography-computed tomography standardized uptake values in clinical practice and assessing response to therapy. *Semin. Ultrasound CT MR*, **31**, 496–505.
79. Wang, X., Sarkar, A., Cicchetti, F., Yu, M., Zhu, A., Jokivarsi, K., Saint-Pierre, M. and Brownell, A.L. (2005) Cerebral PET imaging and histological evidence of transglutaminase inhibitor cystamine induced neuroprotection in transgenic R6/2 mouse model of Huntington's disease. *J. Neurol. Sci.*, **231**, 57–66.
80. Stack, E.C., Kubilus, J.K., Smith, K., Cormier, K., Del Signore, S.J., Guelin, E., Ryu, H., Hersch, S.M. and Ferrante, R.J. (2005) Chronology of behavioral symptoms and neuropathological sequela in R6/2 Huntington's disease transgenic mice. *J. Comp. Neurol.*, **490**, 354–370.
81. Gray, M., Shirasaki, D.I., Cepeda, C., Andre, V.M., Wilburn, B., Lu, X.H., Tao, J., Yamazaki, I., Li, S.H., Sun, Y.E. *et al.* (2008) Full-length human mutant huntingtin with a stable polyglutamine repeat can elicit progressive and selective neuropathogenesis in BACHD mice. *J. Neurosci.*, **28**, 6182–6195.
82. Mantovani, S., Gordon, R., Li, R., Christie, D.C., Kumar, V. and Woodruff, T.M. (2016) Motor deficits associated with Huntington's disease occur in the absence of striatal degeneration in BACHD transgenic mice. *Hum. Mol. Genet.*, **25**, 1780–1791.
83. Menalled, L., El-Khodor, B.F., Patry, M., Suarez-Farinas, M., Orenstein, S.J., Zahasky, B., Leahy, C., Wheeler, V., Yang, X.W., MacDonald, M. *et al.* (2009) Systematic behavioral evaluation of Huntington's disease transgenic and knock-in mouse models. *Neurobiol. Dis.*, **35**, 319–336.
84. Pouladi, M.A., Stanek, L.M., Xie, Y., Franciosi, S., Southwell, A.L., Deng, Y., Butland, S., Zhang, W., Cheng, S.H.,

Shihabuddin, L.S. *et al.* (2012) Marked differences in neurochemistry and aggregates despite similar behavioural and neuropathological features of Huntington disease in the full-length BACHD and YAC128 mice. *Hum. Mol. Genet.*, **21**, 2219–2232.
85. Southwell, A.L., Ko, J. and Patterson, P.H. (2009) Intrabody gene therapy ameliorates motor, cognitive, and neuropathological symptoms in multiple mouse models of Huntington's disease. *J. Neurosci.*, **29**, 13589–13602.
86. Imai, Y., Ibata, I., Ito, D., Ohsawa, K. and Kohsaka, S. (1996) A novel gene iba1 in the major histocompatibility complex class III region encoding an EF hand protein expressed in a monocytic lineage. *Biochem. Biophys. Res. Commun.*, **224**, 855–862.
87. Ito, D., Imai, Y., Ohsawa, K., Nakajima, K., Fukuuchi, Y. and Kohsaka, S. (1998) Microglia-specific localisation of a novel calcium binding protein, Iba1. *Brain. Res. Mol. Brain Res.*, **57**, 1–9.
88. Ridley, A., Paterson, H., Johnston, C., Diekmann, D. and Hall, A. (1992) The small GTP-binding protein rac regulates growth factor-induced membrane ruffling. *Cell*, **70**, 401–410.
89. Zhang, J.M. and An, J. (2007) Cytokines, inflammation, and pain. *Int. Anthesiol. Clin.*, **45**, 27–37.
90. Lavisse, S., Guillermier, M., Herard, A.S., Petit, F., Delahaye, M., Van Camp, N., Ben Haim, L., Lebon, V., Remy, P., Dolle, F. *et al.* (2012) Reactive astrocytes overexpress TSPO and are detected by TSPO positron emission tomography imaging. *J. Neurosci.*, **32**, 10809–10818.
91. Banati, R.B., Newcombe, J., Gunn, R.N., Cagnin, A., Turkheimer, F., Heppner, F., Price, G., Wegner, F., Giovannoni, G., Miller, D.H. *et al.* (2000) The peripheral benzodiazepine binding site in the brain in multiple sclerosis: quantitative in vivo imaging of microglia as a measure of disease activity. *Brain*, **123**, 2321–2337.
92. Vagner, T., Dvorzhak, A., Wojtowicz, A.M., Harms, C. and Grantyn, R. (2016) Systemic application of AAV vectors targeting GFAP-expressing astrocytes in Z-Q175-KI Huntington's disease mice. *Mol. Cell. Neurosci.*, **77**, 76–86.
93. Tong, X., Ao, Y., Faas, G.C., Nwaobi, S.E., Xu, J., Haustein, M.D., Anderson, M.A., Mody, I., Olsen, M.L., Sofroniew, M.V. *et al.* (2014) Astrocyte Kir4.1 ion channel deficits contribute to neuronal dysfunction in Huntington's disease model mice. *Nat. Neurosci.*, **17**, 694–703.
94. Venneti, S., Wang, G., Nguyen, J. and Wiley, C.A. (2008) The positron emission tomography ligand DAA1106 binds with high affinity to activated microglia in human neurological disorders. *J. Neuropathol. Exp. Neurol.*, **67**, 1001–1010.
95. Andre, R., Carty, L. and Tabrizi, S.J. (2016) Disruption of immune cell function by mutant huntingtin in Huntington's disease pathogenesis. *Curr. Opin. Pharmacol.*, **26**, 33–38.
96. Mattson, M.P. and Camandola, S. (2001) NF-kappaB in neuronal plasticity and neurodegenerative disorders. *J. Clin. Invest.*, **107**, 247–254.
97. Khoshnan, A., Ko, J., Watkin, E.E., Paige, L.A., Reinhart, P.H. and Patterson, P.H. (2004) Activation of the IkappaB kinase complex and nuclear factor-kappaB contributes to mutant huntingtin neurotoxicity. *J. Neurosci.*, **24**, 7999–8008.
98. Trager, U., Andre, R., Lahiri, N., Magnusson-Lind, A., Weiss, A., Grueninger, S., McKinnon, C., Sirinathsinghji, E., Kahlon, S., Pfister, E.L. *et al.* (2014) HTT-lowering reverses Huntington's disease immune dysfunction caused by NFkappaB pathway dysregulation. *Brain*, **137**, 819–833.
99. Beckers, L., Ory, D., Geric, I., Declercq, L., Koole, M., Kassiou, M., Bormans, G. and Baes, M. (2018) Increased expression of translocator protein (TSPO) marks pro-inflammatory microglia but does not predict neurodegeneration. *Mol. Imaging Biol.*, **20**, 94–102.
100. Karlstetter, M., Nothdurfter, C., Aslanidis, A., Moeller, K., Horn, F., Scholz, R., Neumann, H., Weber, B.H., Rupprecht, R. and Langmann, T. (2014) Translocator protein (18 kDa) (TSPO) is expressed in reactive retinal microglia and modulates microglial inflammation and phagocytosis. *J. Neuroinflammation*, **11**, 3.
101. Bourdiol, F., Toulmond, S., Serrano, A., Benavides, J. and Scatton, B. (1991) Increase in omega 3 (peripheral type benzodiazepine) binding sites in the rat cortex and striatum after local injection of interleukin-1, tumour necrosis factor-alpha and lipopolysaccharide. *Brain Res.*, **543**, 194–200.
102. Wilms, H., Claasen, J., Rohl, C., Sievers, J., Deuschl, G. and Lucius, R. (2003) Involvement of benzodiazepine receptors in neuroinflammatory and neurodegenerative diseases: evidence from activated microglial cells in vitro. *Neurobiol. Dis.*, **14**, 417–424.
103. Bjorkqvist, M., Wild, E.J., Thiele, J., Silvestroni, A., Andre, R., Lahiri, N., Raibon, E., Lee, R.V., Benn, C.L., Soulet, D. *et al.* (2008) A novel pathogenic pathway of immune activation detectable before clinical onset in Huntington's disease. *J. Exp. Med.*, **205**, 1869–1877.
104. Silvestroni, A., Faull, R.L., Strand, A.D. and Moller, T. (2009) Distinct neuroinflammatory profile in post-mortem human Huntington's disease. *Neuroreport*, **20**, 1098–1103.
105. Wyss-Coray, T. (2006) Inflammation in Alzheimer disease: driving force, bystander or beneficial response? *Nat. Med.*, **12**, 1005–1015.
106. Byrne, L.M. and Wild, E.J. (2016) Cerebrospinal fluid biomarkers for Huntington's disease. *J. Huntington's Dis.*, **5**, 1–13.
107. Dalrymple, A., Wild, E.J., Joubert, R., Sathasivam, K., Bjorkqvist, M., Petersen, A., Jackson, G.S., Isaacs, J.D., Kristiansen, M., Bates, G.P. *et al.* (2007) Proteomic profiling of plasma in Huntington's disease reveals neuroinflammatory activation and biomarker candidates. *J. Proteome Res.*, **6**, 2833–2840.
108. Bouwens, J.A., van Duijn, E., Cobbaert, C.M., Roos, R.A., van der Mast, R.C. and Giltay, E.J. (2016) Plasma cytokine levels in relation to neuropsychiatric symptoms and cognitive dysfunction in Huntington's disease. *J. Huntington's Dis.*, **5**, 369–377.
109. Wild, E., Magnusson, A., Lahiri, N., Krus, U., Orth, M., Tabrizi, S.J. and Bjorkqvist, M. (2011) Abnormal peripheral chemokine profile in Huntington's disease. *PLoS Curr.*, **3**, RRN1231.
110. Chang, K.H., Wu, Y.R., Chen, Y.C. and Chen, C.M. (2015) Plasma inflammatory biomarkers for Huntington's disease patients and mouse model. *Brain Behav. Immun.*, **44**, 121–127.
111. Airas, L., Dickens, A.M., Elo, P., Marjamaki, P., Johansson, J., Eskola, O., Jones, P.A., Trigg, W., Solin, O., Haaparanta-Solin, M. *et al.* (2015) In vivo PET imaging demonstrates diminished microglial activation after fingolimod treatment in an animal model of multiple sclerosis. *J. Nucl. Med.*, **56**, 305–310.
112. Tremoleda, J.L., Thau-Zuchman, O., Davies, M., Foster, J., Khan, I., Vadivelu, K.C., Yip, P.K., Sosabowski, J., Trigg, W. and Michael-Titus, A.T. (2016) In vivo PET imaging of the neuroinflammatory response in rat spinal cord injury using

the TSPO tracer [(18)F]GE-180 and effect of docosahexaenoic acid. *Eur. J. Nucl. Med. Mol. Imaging*, **43**, 1710–1722.
113. Sucksdorff, M., Rissanen, E., Tuisku, J., Nuutinen, S., Paavilainen, T., Rokka, J., Rinne, J. and Airas, L. (2017) Evaluation of the effect of fingolimod treatment on microglial activation using serial PET imaging in multiple sclerosis. *J. Nucl. Med.*, **58**, 1646–1651.
114. Waerzeggers, Y., Monfared, P., Viel, T., Winkeler, A. and Jacobs, A.H. (2010) Mouse models in neurological disorders: applications of non-invasive imaging. *Biochim. Biophys. Acta*, **1802**, 819–839.
115. Sattarivand, M., Armstrong, J., Szilagyi, G.M., Kusano, M., Poon, I. and Caldwell, C. (2013) Region-based partial volume correction techniques for PET imaging: sinogram implementation and robustness. *Int. J. Mol. Imaging*, **2013**, 1.
116. Dickstein, L.P., Zoghbi, S.S., Fujimura, Y., Imaizumi, M., Zhang, Y., Pike, V.W., Innis, R.B. and Fujita, M. (2011) Comparison of 18F- and 11C-labeled aryloxyanilide analogs to measure translocator protein in human brain using positron emission tomography. *Eur. J. Nucl. Med. Mol. Imaging*, **38**, 352–357.
117. Chauveau, F., Boutin, H., Van Camp, N., Dolle, F. and Tavitian, B. (2008) Nuclear imaging of neuroinflammation: a comprehensive review of [11C]PK11195 challengers. *Eur. J. Nucl. Med. Mol. Imaging*, **35**, 2304–2319.
118. Hamelin, L., Lagarde, J., Dorothee, G., Leroy, C., Labit, M., Comley, R.A., de Souza, L.C., Corne, H., Dauphinot, L., Bertoux, M. *et al.* (2016) Early and protective microglial activation in Alzheimer's disease: a prospective study using 18F-DPA-714 PET imaging. *Brain*, **139**, 1252–1264.
119. Owen, D.R., Yeo, A.J., Gunn, R.N., Song, K., Wadsworth, G., Lewis, A., Rhodes, C., Pulford, D.J., Bennacef, I., Parker, C.A. *et al.* (2012) An 18-kDa translocator protein (TSPO) polymorphism explains differences in binding affinity of the PET radioligand PBR28. *J. Cereb. Blood Flow Metab.*, **32**, 1–5.
120. Turkheimer, F.E., Rizzo, G., Bloomfield, P.S., Howes, O., Zanotti-Fregonara, P., Bertoldo, A. and Veronese, M. (2015) The methodology of TSPO imaging with positron emission tomography. *Biochem. Soc. Trans.*, **43**, 586–592.
121. Yoder, K.K., Nho, K., Risacher, S.L., Kim, S., Shen, L. and Saykin, A.J. (2013) Influence of TSPO genotype on 11C-PBR28 standardized uptake values. *J. Nucl. Med.*, **54**, 1320–1322.
122. Wild, E.J., Boggio, R., Langbehn, D., Robertson, N., Haider, S., Miller, J.R., Zetterberg, H., Leavitt, B.R., Kuhn, R., Tabrizi, S.J. *et al.* (2015) Quantification of mutant huntingtin protein in cerebrospinal fluid from Huntington's disease patients. *J. Clin. Invest.*, **125**, 1979–1986.
123. Kotrcova, E., Jarkovska, K., Valekova, I., Zizkova, M., Motlik, J., Gadher, S.J. and Kovarova, H. (2015) Challenges of Huntington's disease and quest for therapeutic biomarkers. *Proteomics Clin. Appl.*, **9**, 147–158.
124. Rocha, N.P., Ribeiro, F.M., Furr-Stimming, E. and Teixeira, A.L. (2016) Neuroimmunology of Huntington's disease: revisiting evidence from human studies. *Mediators Inflamm.*, **2016**, 1.
125. Simmons, D.A., Mehta, R.A., Lauterborn, J.C., Gall, C.M. and Lynch, G. (2011) Brief ampakine treatments slow the progression of Huntington's disease phenotypes in R6/2 mice. *Neurobiol. Dis.*, **41**, 436–444.
126. Knowles, J.K., Rajadas, J., Nguyen, T.V., Yang, T., LeMieux, M.C., Vander Griend, L., Ishikawa, C., Massa, S.M., Wyss-Coray, T. and Longo, F.M. (2009) The p75 neurotrophin receptor promotes amyloid-beta(1-42)-induced neuritic dystrophy in vitro and in vivo. *J. Neurosci.*, **29**, 10627–10637.
127. Knowles, J.K., Simmons, D.A., Nguyen, T.V., Vander Griend, L., Xie, Y., Zhang, H., Yang, T., Pollak, J., Chang, T., Arancio, O. *et al.* (2013) A small molecule p75NTR ligand prevents cognitive deficits and neurite degeneration in an Alzheimer's mouse model. *Neurobiol. Aging*, **34**, 2052–2063.
128. Lartey, F.M., Ahn, G.O., Shen, B., Cord, K.T., Smith, T., Chua, J.Y., Rosenblum, S., Liu, H., James, M.L., Chernikova, S. *et al.* (2014) PET imaging of stroke-induced neuroinflammation in mice using [18F]PBR06. *Mol. Imaging Biol.*, **16**, 109–117.
129. Gandelman, M.S., Baldwin, R.M., Zoghbi, S.S., Zea-Ponce, Y. and Innis, R.B. (1994) Evaluation of ultrafiltration for the free-fraction determination of single photon emission computed tomography (SPECT) radiotracers: beta-CIT, IBF, and iomazenil. *J. Pharm. Sci.*, **83**, 1014–1019.
130. James, M.L., Shen, B., Zavaleta, C.L., Nielsen, C.H., Mesangeau, C., Vuppala, P.K., Chan, C., Avery, B.A., Fishback, J.A., Matsumoto, R.R. *et al.* (2012) New positron emission tomography (PET) radioligand for imaging sigma-1 receptors in living subjects. *J. Med. Chem.*, **55**, 8272–8282.
131. Franklin, K. and Paxinos, G. (2008) *The Mouse Brain in Stereotaxic Coordinates*. Elsevier, Inc., New York.